8-9-2014

FLOW DYNAMICS IN THE TRANSITION ZONE FROM ESTUARINE TIDAL TO FLUVIAL REGIME IN THE SANTEE RIVER, SC, USA

Legna M. Torres-Garcia
University of South Carolina - Columbia

FLOW DYNAMICS IN THE TRANSITION ZONE FROM ESTUARINE TIDAL TO FLUVIAL REGIME IN THE SANTEE RIVER, SC, USA

by

Legna M. Torres-Garcia

Bachelor of Science
University of Puerto Rico at Mayaguez, 2006

Master of Science
University of South Carolina, 2009

Submitted in Partial Fulfillment of the Requirements

For the Degree of Master of Science in

Geological Sciences

College of Arts and Sciences

University of South Carolina

2014

Accepted by:

Alexander E. Yankovsky, Director of Thesis

Raymond Torres, Reader

George Voulgaris, Reader

Lacy Ford, Vice Provost and Dean of Graduate Studies

DEDICATION

I dedicate this to my parents Miguel and Elis who made me the women I am today. They guided me and supported me every step of the way. To my husband Christopher for reminding me always that there is light at the end of the tunnel. Lastly, to my son Tiago who is my little bundle of joy and my daily ray of sunshine.

ACKNOWLEDGEMENTS

First, I would like to thank my advisor Dr. Alexander E. Yankovsky for his support and guidance in this project.

I would like to thank my committee members Dr. George Voulgaris and Dr. Raymond Torres for their time and feedback.

I would like to thank the United States Geological Survey for providing me with data for my study site. This study was supported by NSF grant EAR-1053299.

I would like to thank Dr. McFadden and Mrs. Gettone for making me part of SEAGEP, but more than that, for supporting me in every way and making me feel a part of their family.

I want to thank my parents for giving me their unconditional support. I want to thank my husband Chris for his unconditional help all these years. Thank you for helping me to improve my English. I want to thank my sisters Johannaliz, Eli, Marelis and Lydian for creating amazing memories and making me part of this united family.

I would like to thank Nirnimesh Kumar and Yan Jia for their help and guidance with computer programing, and our discussions about science. I want to thank Cristian Monaco for helping me to retrieve instruments from the water when we thought we had lost them. I want to thank my friends and colleagues Jessica Chasseareau, Nehe Kyungho Jeon, Xi Chen and Alex Frank for their help.

Lastly, I would like to thank Oscar Lopez for being there since the beginning of this journey.

ABSTRACT

Estuaries are important systems that link fresh, inland waters to oceanic salt water, where they act to deliver large amounts of nutrients, sediments and pollutants into the ocean. Traditionally, the study of estuarine systems has been marked by difficulty owing to the complex hydrodynamics influenced by strong bathymetric changes, changes in tidal range, intricate geomorphology, among other factors; thus beginning to unravel the complexities of estuarine hydrodynamics will help to illuminate the nature of estuaries as well as to provide a foundation for their further study. In this study I focus on the transition zone from tidal to fluvial regime, which is defined as an area where tidal and river discharges are comparable. Recently, the transition zone has been the focus of attention as an important region within an estuary.

Tides are subject to frictional dissipation as they propagate inland through estuaries and river channels. Previous studies suggest that there is an enhanced tidal dissipation in the transition zone from a tidal to fluvial regime when the tidal flux and river discharge become comparable. The aim of this study is to understand the kinematics and dynamics within the transition zone. In particular, I hypothesize that there is an enhanced tidal dissipation in the transition zone due to (i) additive effects of tidal and river currents subject to the quadratic bottom friction, and (ii) to the presence of variable topography and enhanced bathymetric gradients in the transition zone. I analyzed time series of velocity profiles and bottom pressure that resolve the along-channel depth-averaged momentum balance in the transition zone of the Santee River, SC, USA. The following momentum

balance terms are estimated: inertia (local acceleration), along-channel advective acceleration, pressure gradient, and bottom friction terms. Instruments were deployed in a 1-km long river reach characterized by a decreasing depth in the upstream direction from over 4 m to less than 2 m. Tides in the study area are predominantly semi-diurnal, flood-dominant. The leading terms in the depth-averaged momentum balance are found to be inertia, pressure gradient, and bottom friction. The pressure gradient and inertia dominate the momentum balance during the flood and subsequent current reversal from flood to ebb. However, during the ebb the pressure gradient is nearly balanced by bottom friction. A dissipative term is defined as a residual of inertia, advection, and pressure gradient force terms. I found that the dissipative term is comparable with the bottom friction term under steady river discharge. However, the bottom friction term underestimates the dissipative term when the river discharge exhibits abrupt variations. This yields a record-mean with a linear regression slope of 0.54. I hypothesize that the lateral eddy viscosity also contributes to tidal dissipation, especially when the pressure gradient force increases. Although tides are flood-dominant, most of the dissipation occurs during the ebb due to a superposition of comparable fluvial and tidal currents.

TABLE OF CONTENTS

LIST OF FIGURES

LIST OF SYMBOLS

C_d	Drag coefficient.
Diss	Dissipative Term: sum of inertia, advective acceleration and pressure gradient force.
$\mathcal{F}_x$	Horizontal transfer of momentum along *x*.
$\mathcal{F}_y$	Horizontal transfer of momentum along *y*.
g	Acceleration due to gravity.
h	Water depth.
k	Von Kàrmán's constant.
η	*P*erturbation of free surface for horizontal level.
ρ	Water density.
τ	Turbulent shear stress.
τ_b	Bottom friction.
u_*	Frictionvelocity.
u	Depth-averaged along-channel velocity.
v	Depth-averaged across-channel velocity.
x	Along-channel coordinate.
y	Across-channel coordinate.
z	Height.
z_o	Roughness height.

List of Abbreviations

BBL ..... Bottom Boundary Layer

HR ..... High Resolution

LPF ..... Low-Pass Filter

LR ..... Low Resolution

PGF ..... Pressure Gradient Force

USGS ..... United States Geology Survey

CHAPTER 1

INTRODUCTION

1.1 Background

Estuaries are important systems that link fresh, inland river water with oceanic salt water, and act as conduits for large amounts of nutrients, sediments and pollutants being delivered into the ocean (Pricthard, 1967). Moreover, the study of estuaries helps to elucidate many aspects of oceanographic processes including tidal processes, residual subtidal estuarine currents, as well as sediment transport. As the tides propagate inland through an estuary they exhibit important transformations: (i) there is an increase in tide amplitude due to the decrease of the estuarine cross-sectional area; and (ii) as the tidal wave continues to travel upstream it decays due to bottom friction and energy is lost. In many cases these two tendencies balance one another and the approximation of an "ideal" estuary can be made (e.g., Prandle, 2009). In order to comprehensively understand tidal dynamics, there are numerous variables to consider, and, in particular, when strong bathymetric, finite amplitude and bottom friction are taken into account, the dynamics become difficult to solve analytical.

Estuaries are divided into three major areas (Figure 1.1), (i) lower estuary, marine dominated region; (ii) central region, where there is usually an increase in convergence of the estuary; and (iii) the inner river-dominated region or upper estuary, characterized by freshwater dominance, but subject to tidal influence (Dalrymple, 1992). Since the inner river-dominated region is composed only of fresh water, it allows us to assume that the tide

propagates upstream in the form of free wave enabling the use of wave equations to describe flow dynamics. As the tidal waves travel upstream the water flow changes from tidal dominant bidirectional to unidirectional river (fluvial) dominant. Tidal waves at the mouth often behave as linear waves and as a result they exert a symmetric bottom stress. As the wave moves upstream tidal fluxes gradually decrease with the upstream distance and as they reach the upper estuary they become comparable with river discharge, this area is defined as the transition zone (i.e., Yankovsky et al., 2012). Tidal waves propagating inland and reaching this zone are characterized by an addition of fluvial and tidal flux (Horrevoets et al., 2004) subject to quadratic bottom friction (Prandle, 2009; Godin, 1998). Since tidal fluxes are much greater compared to river discharge in low estuaries near the mouth, the fluvial effect on tidal dynamics is often ignored, however in the transition zone it is an important variable. I seek to demonstrate that the river discharge can have a considerable influence on tidal damping in the transition zone.

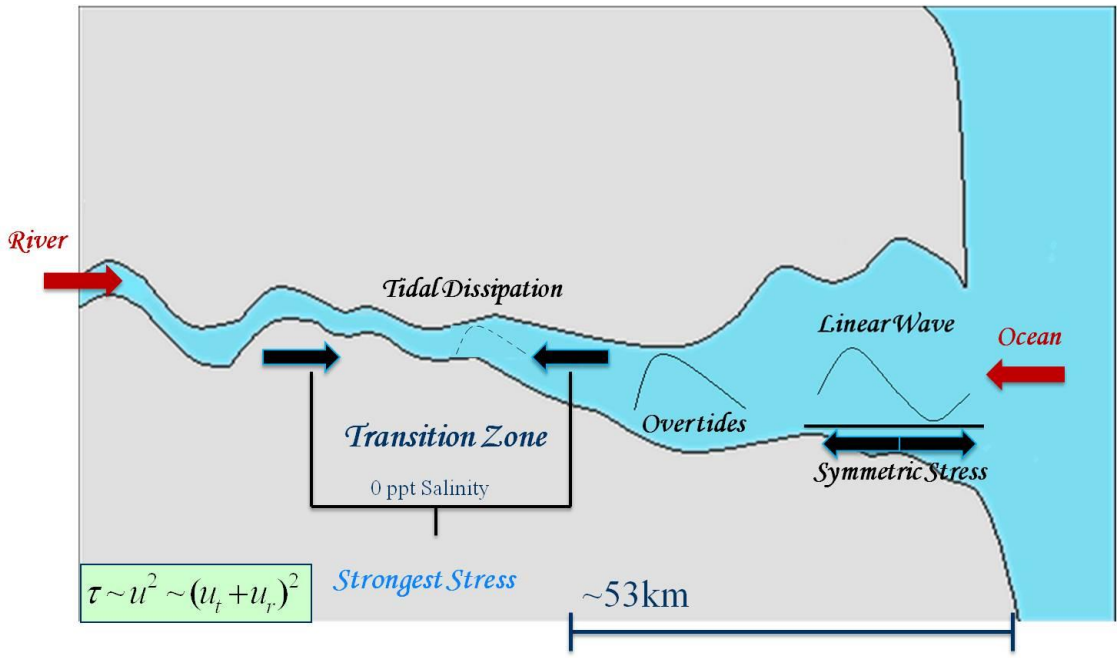

Figure 1.1 A schematic diagram that describes the dynamics of a tidal wave when it enters from the mouth and reaches the upper estuary.

There has been gathering interest to study tidal dynamics and their importance in different regions of estuaries. Many studies have been conducted in the lower part of estuaries to understand the physical exchanges, the interaction between freshwater and salinity, bathymetry changes and the mechanisms in forcing currents at tidal and subtidal regimes (Prandle, 2003). In recent years a few studies have been conducted in upper estuaries, past the salt intrusion limit, where residual currents and mass transport driven by gradients in salinity are not present (Buschman et al., 2009; Hoitink et al., 2009; Sassi et al., 2011). These studies discussed tidal processes in the transition zone, however they focused on subtidal fluctuations, tidally averaged and not on the tidal cycle.

As tides propagate upstream they become asymmetric and their distortion is related to finite amplitude effects and the generation of overtides (Blanton, 2002; Lanzoni and Seminara, 1998). Overtides cause a change in the sinusoidal behavior, which results, in the case of flood-dominant regime, in a short-lasting stronger flood and weaker but long-lasting ebb. Energy dissipation occurs as a consequence of long-lasting ebb in the transition zone, where there is an addition of fluvial and tidal velocities. The tidal distortion is a prominent characteristic of a flood-dominant estuary. When M_2 is the dominant semidiurnal constituent, M_4 is the largest quarter-diurnal tide formed within the estuary (Speer, Aubrey, et al., 1991). The ratio of M_4 and M_2 shows a highly tidal distortion in the transition zone.

Furthermore, the importance of the interaction between fluvial and tidal currents (Horrevoets et al., 2004; LeBlond, 1979; Godin, 1991; Buschman et al., 2009) is being acknowledged. For example, Wong and Sommerfield (2009) presented an observational study in the upper Delaware estuary where they found that there is, in fact, a tidal current

amplification at the upper estuary. They also showed the importance of the river discharge in relation to forcing the mean flow.

A key feature of the flow dynamics of the transition zone is the along-channel momentum balance, which can be used to describe the general aspects of hydrodynamics of the upper estuary. There is an agreement in the importance of the observational work to resolve momentum balance, although it presents a challenge due to the complexity of the estuarine tidal dynamics (Trowbridge et al., 1999). My major research goal is to study the tidal dynamics in the upper estuary with an emphasis on tidal interactions with abrupt bathymetric gradients while considering river discharge. Other studies showed that channel geometry produced variability in tidal current, amplitude and phases (Seim et al., 2006).

Tidal dynamics in the transition zone can be explained by estimating the along-channel depth-averaged momentum balance. The along-channel momentum balance equation is comprised by linear and no-linear terms. It is known that the tidal wave non-linearity is primarily associated with the advection and bottom friction, and results in the generation of overtides (Lanzoni & Seminara, 1998). Theoretical and observational work has been previously performed to describe tidal dynamics; however these studies are often based on simplifying assumptions. Prandle (2009) describes theoretical tidal dynamics using the equations of motion. He explains the role of amplitude, bed friction, inertia and how they vary depending on different characteristics. Savenije, Toffolon, et al. (2008) used analytical solutions of these equations in a one-dimensional form to describe tidal wave propagation, but ignored the downstream velocity component from river input. When mass conservation and momentum balance equations are used there are non-linear terms that

explain the tidal behavior. Jay (1991) explains these effects, friction and variable topography, on tidal wave propagation. There are a few studies that are based on strongly convergent channels; however these studies linearized the friction term (Friedrichs & Aubrey, 1994). An observational example is shown by Trowbridge et al. (1998) where they studied a straight section of the lower Hudson estuary to obtain the bottom stress using the law of the wall and to resolve along-channel momentum balance. Sassi et al., 2011 reveals the influence of side wall effects on velocity profiles in a tidal river. Their study provides progress towards understanding momentum balance; however there still remain numerous unresolved aspects of momentum balance, including what happens in the transition zone in relation to river discharge and tidal dissipation and the relation between energy loss and geomorphology.

The main objective of this study if to resolves the along-channel depth-averaged momentum balance equation by observational data at the transition zone of the Santee River, South Carolina, USA. I resolved inertia, advection of momentum, bottom friction and pressure gradient terms within the tidal cycle. I sought observational evidence for the enhanced bottom friction due to the interplay between fluvial and tidal currents, as well as the role of the dissipative term (bottom friction and horizontal transfer of momentum). The transition zone is characterized by strong tidal dissipation (Yankovsky et al., 2012). I hypothesized that there is an enhanced tidal dissipation in the transition zone due to (i) additive effects of tidal and river currents subject to the quadratic bottom friction, and (ii) to the presence of variable topography and enhanced bathymetric gradients in the transition zone.

CHAPTER 2

DATA AND METHODOLOGY

2.1 STUDY SITE

The experiment was conducted in the freshwater reach of the Santee River on July 16 to August 18, 2010. The center of the study area was approximately 53 km upstream from the river mouth (Figure 2.1). The Santee River is a coastal plain river approximately 230 km long formed by the confluence of the Wateree and Congaree rivers southeast of Columbia, SC. The Santee River provided principal drainage for the coastal areas of southeastern South Carolina. Downstream of the study site, the Santee River splits into two channels: the North Santee and the South Santee, located 10 miles (16 km) from the mouth, reaching the Atlantic Ocean south of Georgetown, SC. The Santee River discharge is regulated by the Lake Marion and (to a lesser degree) Lake Moultrie dams.

The data were supplemented by USGS observations of stream flow velocity and river discharge from the gauging station 02171700, near Jamestown, SC (Figure 2.1) on the Alt 17 bridge (33º18'17"N and 79º40'42"W) and approximately 57 km downstream of the Lake Marion dam, 24 km downstream of the Lake Moultrie diversion, and 55 km upstream of the mouth. The station consists of a SonTek Argonaut SL velocimeter that samples at 15-minute intervals. According to the USGS data record spanning the years 2000 through 2010 the average discharge was 202.2 m^3s^{-1}, with a monthly low of 18.2 m^3s^{-1} and a monthly high of 1,323.8 m^3s^{-1}. During the end of July through the end of August 2010 low discharge conditions were observed, with tidally-averaged discharge varying

from 23.3 m^3s^{-1} - 42.7 m^3s^{-1}. The USGS data presented in this study comprise river discharge and streamflow data for March to October 2008 and 2010 thus overlapping periods of the current meter deployments.

2.2 OBSERVATIONAL DATA

There were two different equipment arrays set up in the Santee River: the first one, that I will briefly make reference to, from 2008 and the second one which this project is based on from 2010. The 2008 deployment consisted of two upward-looking Aquadopp current profiles mounted on bottom tripods and separated by approximately 6 km along-channel distance. The upstream location (R) and downstream location (S) record-mean water depths were 1.78 m and 3.27 m respectively (shown in green in Figure 2.2). A detailed description of the 2008 deployment is discussed by Yankovsky et al. (2012).

The 2010 array consisted of three bottom tripods deployed along-channel axis (Figure 2.2). The along-channel extension of the array was slightly less than 900 m, while the USGS gauge station was approximately 1 km further upstream (Figure 2.2). Within the study site, the channel exhibits some curvature and its depth decreases in the upstream direction from ~5 m to ~2 m under the observed low-discharge conditions. Instruments were deployed close to the thalweg and were set to record measurements for approximately one month (July 16 to August 18, 2010). Time of deployment is measured as starting from July 16, 2010, 14:00 (local daylight saving time).

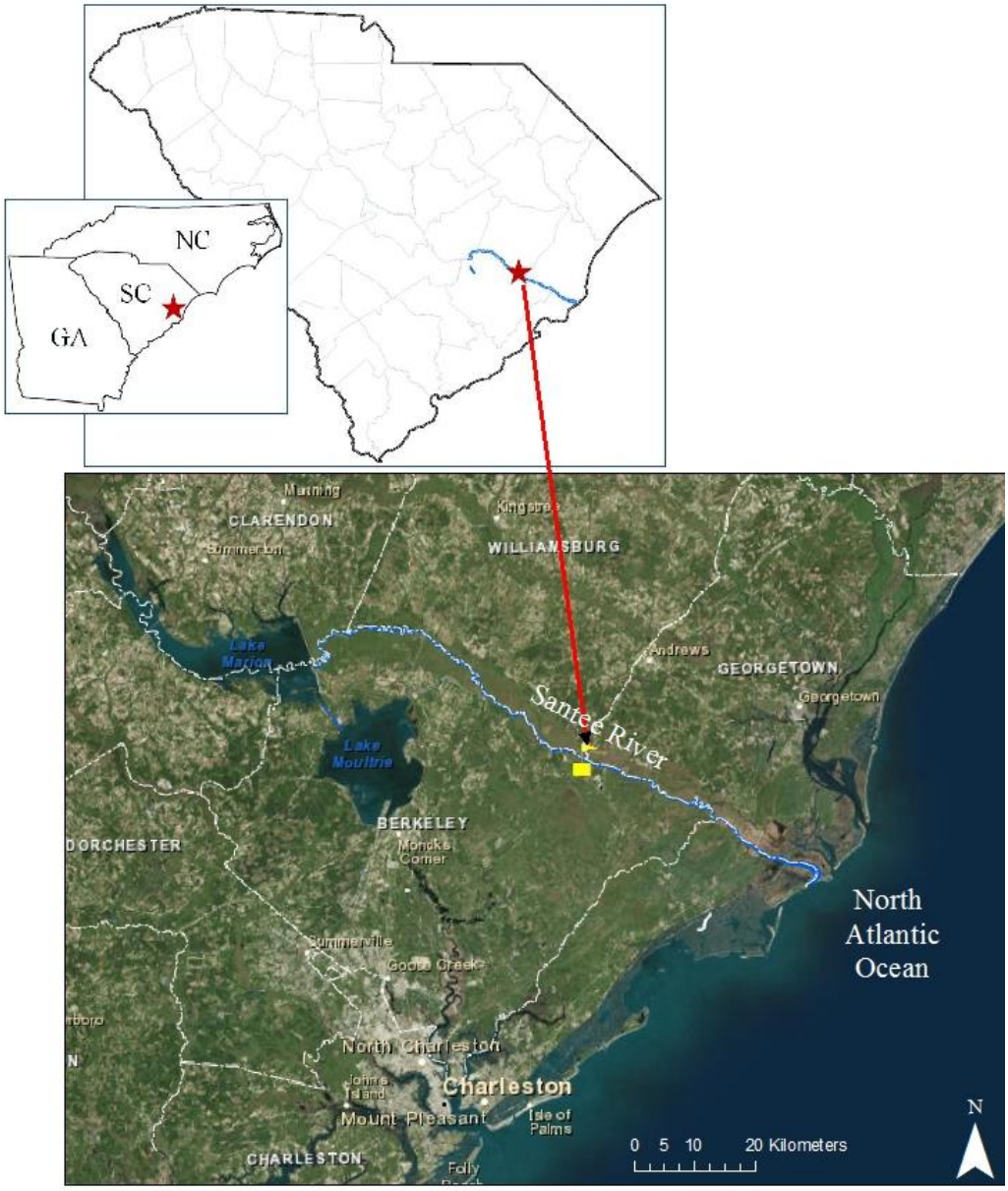

Figure 2.1 Study area in the Santee River, South Carolina, USA.

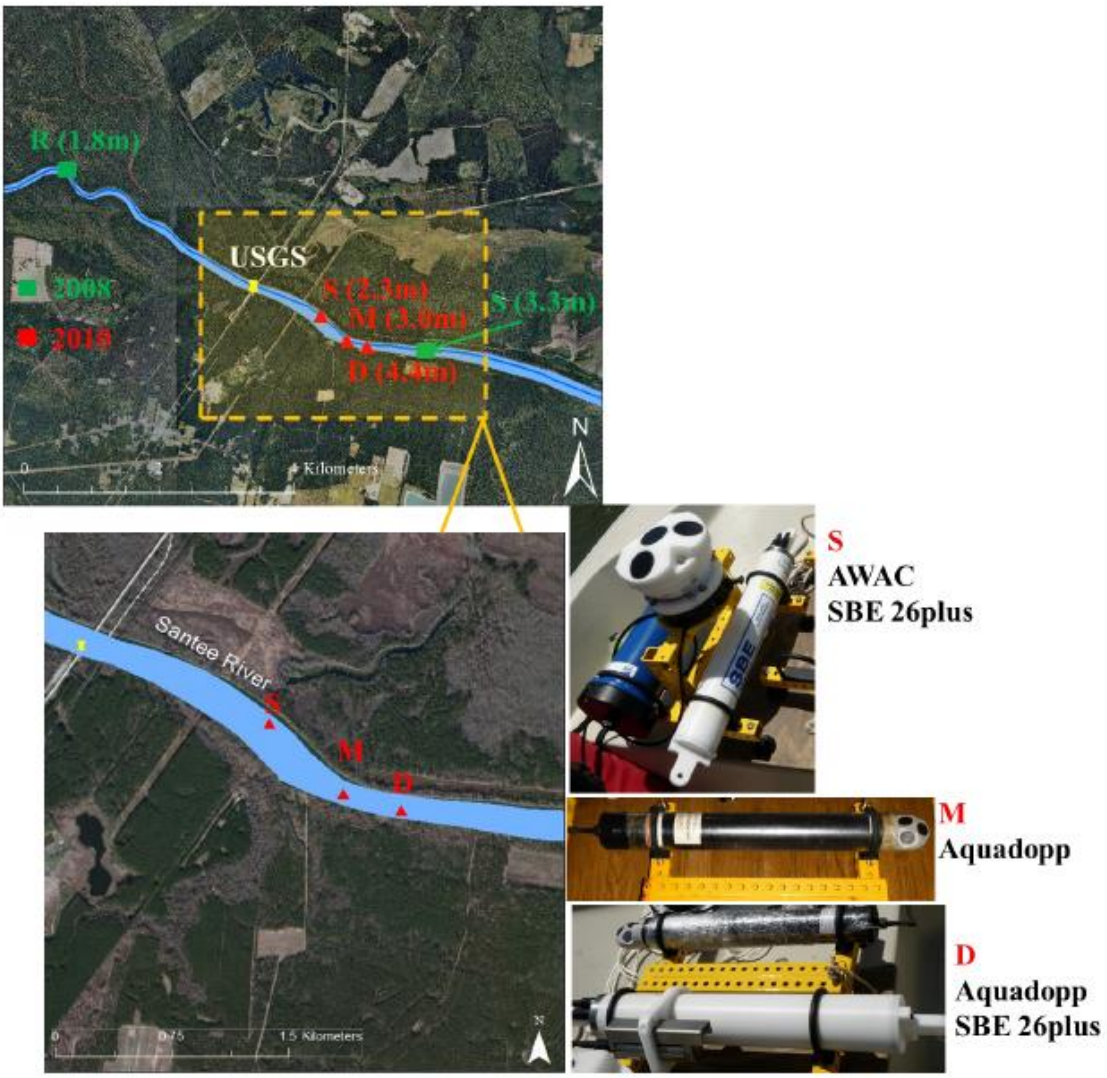

Figure 2.2 Map of the study area. The top panel shows the instrument deployment sites in 2008 (green triangles) and 2010 (red triangles); the corresponding record-mean depth is in parentheses. Yellow pin points the USGS gauging station. The lower panel shows a closer look of the study area and the lower right side shows the instruments deployed at each location.

A Nortek Acoustic Wave and Current recorder (AWAC) and a SBE 26plus Seagauge Wave and Tide Recorder were deployed at the shallowest location (position S, Figure 2.2), with a record-mean water depth of ~2.3 m. The AWAC was configured to resolve the mean flows by measuring three-dimensional flow velocities throughout the water column at a rate of 1 Hz for 120 s every 15 minutes; each 120 s sampling was

internally averaged. The transducer was 0.38 m above the river bed, with a blanking distance of 0.40 m and bin size of 0.5 m. A high resolution Nortek Aquadopp Current Profiler, hereafter referred to as "HR", was deployed at the middle location (marked with M in Figure 2.2) with a record-mean water depth of ~3.0 m. The instrument sampled the lower half of the water column with the same sampling scheme as the AWAC. The transducer was placed 0.13 m above the river bed with a blanking distance of 0.04 m, and the velocity profile consisted of 23 cells with a bin size of 0.05 m. A Nortek Aquadopp Current Profiler, hereafter referred to as "LR" (lower resolution), and a SBE 26plus Conductivity Seagauge Wave and Tide Recorder were deployed at the deepest location, marked with D in Figure 2.2, with a record-mean water depth ~4.4 m. The LR Aquadopp sampled more than half of the water column with the velocity profile consisting of 25 cells, each 0.10 m high. The transducer was 0.13 m above the bed and the blanking distance was 0.20 m. All the pressure sensors of the current profilers were adjusted to atmospheric pressure (set to zero) at the moment of deployment. However, as there was a lack of a barometric pressure record for the study site, and since the atmospheric pressure fluctuated through the period of deployment, I could not infer an accurate water depth through the duration of the measurements. The separations between S and M as well as M and D were 540 m and 320 m, respectively. The SBE 26plus yielded the bottom pressure records with a higher precision required for the along-channel pressure gradient estimate than the AWAC and Aquadopp Current Profilers. The conductivity sensor at location D allowed me to confirm a 0 ppt salinity at the study site.

Bathymetry measurements could not be conducted during the experiment due to the low discharge conditions. The bathymetry survey was done on March 11-12, 2013 when

the discharge was higher making most of the channel to be accessible with a small boat. Tidally averaged discharge recorded at the USGS gauging station 02171700 during the bathymetric survey was 170 - 242 m^3s^{-1} with corresponding tidal fluctuations in stage of 0.55 m, although current reversals did not occur. In this survey the river free surface elevation referenced to the NAVD88 datum, and the water depth was measured. The bathymetry was obtained by subtracting the water depth from the free surface elevation (Figure 2.3).

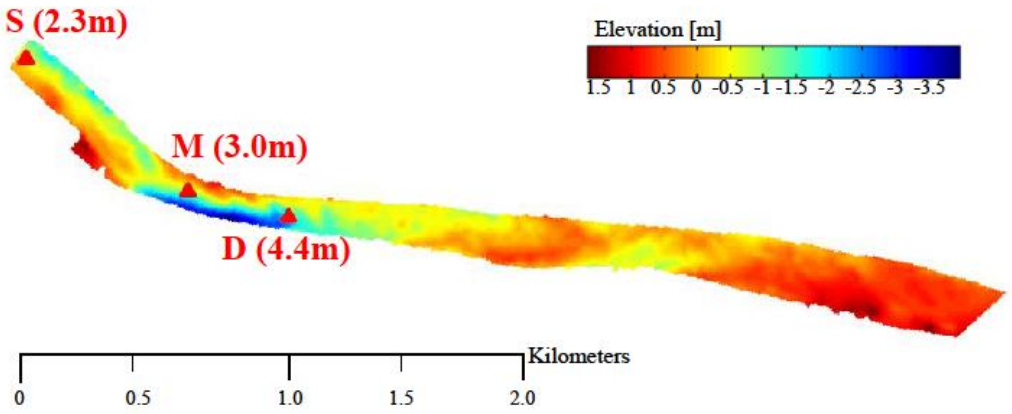

Figure 2.3 Bathymetry of the study area referenced to the NAVD88 datum.

Cross-sectional areas for locations S, M and D were calculated using depth values corresponding to transects where instruments were deployed from the bathymetric survey (survey measurements were done with 1 m separation). I determined the average stage for the time interval of the 2010 deployment from the USGS gage station 02171700. I also

determined the instantaneous stage at the moment of bathymetric measurements at each transect. A Δh (difference between 2010 and 2013 stage measurements) was calculated and adjusted to obtain the water depth across the channel. Figure 2.4 shows the values for the cross-sectional areas calculated. In general there is a convergence at the central location: a decrease in cross-sectional areas from S to M and subsequently an increase from M to D. This result might indicate the potential importance of the advective acceleration terms in this region.

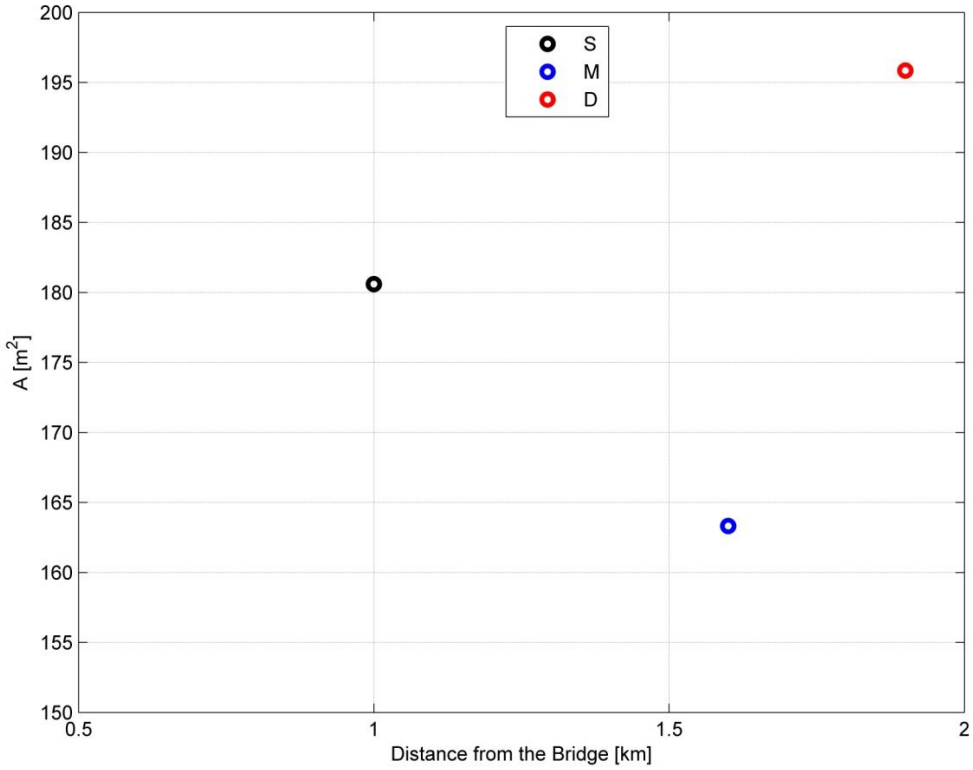

Figure 2.4 Cross-sectional areas for S, M and D locations.

2.3 DATA PROCESING

The time series data recorded were low-pass filtered in order to remove high frequency noise. A Gaussian low-pass filter (LPF) was applied to retain oscillations with periods longer than 1 hr. Furthermore, I subtracted a record-mean value from the SBE 26plus bottom pressure time series. As the first step in the data analysis, I compared the u (eastward) and v (northward) components of the velocity for the Aquadopp at location M and D; and for AWAC at location S (Figure 2.5). I defined the direction of the along-channel velocity component as the direction of the principal axis velocity component [*Emery and Thomson* (2001)], positive downstream (seaward). Furthermore, I determined the minor axis and principal axis to determine alignment between each other as well as standard deviation to ensure u >> v. Figure 2.6 shows an example for cell 19 (1.12 m) which corresponds to the highest elevation sampled at M location. The standard deviation values for the principal and minor axis were 0.0821 and 0.005, respectively. Figure 2.6 shows an alignment with the along-channel direction. For comparison, I also determined the recorded mean velocity direction (see Table 2.1). Both estimates are in good agreement at all three locations indicating alignment of tidal (oscillatory) and river (mean) current velocities. The reference cells used for these estimates correspond to the approximate middle of the water column for each measurement site. I used the following cells: AWAC cell 1 (1.28 m), HR Aquadopp cell 19 (1.12 m) and LR Aquadopp cell 18 (2.12 m).

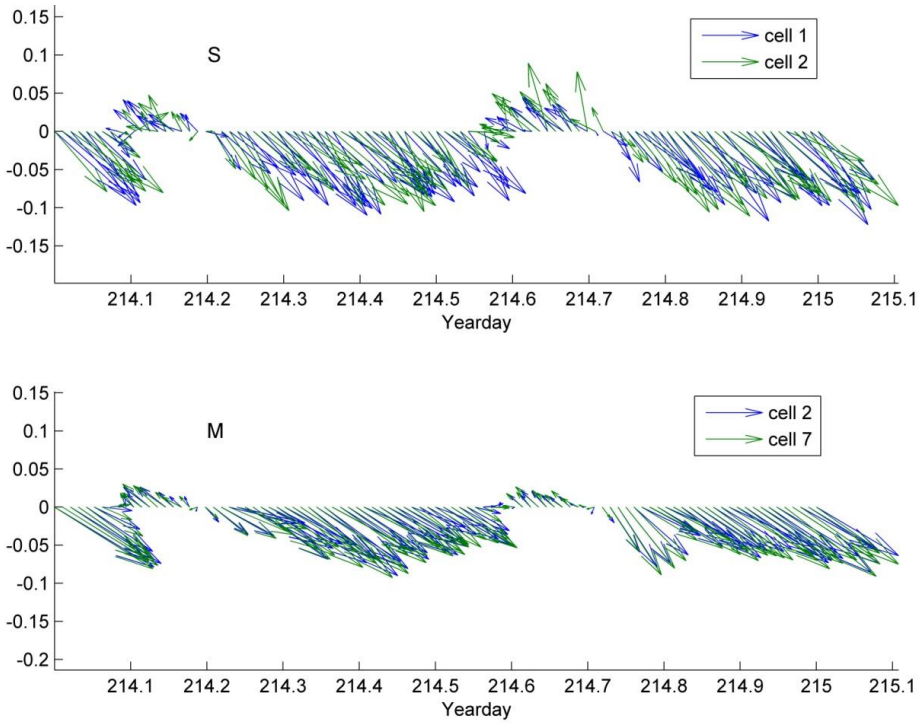

Figure 2.5 Samples of vector time series from two cells of velocity profiles measured at S and M locations.

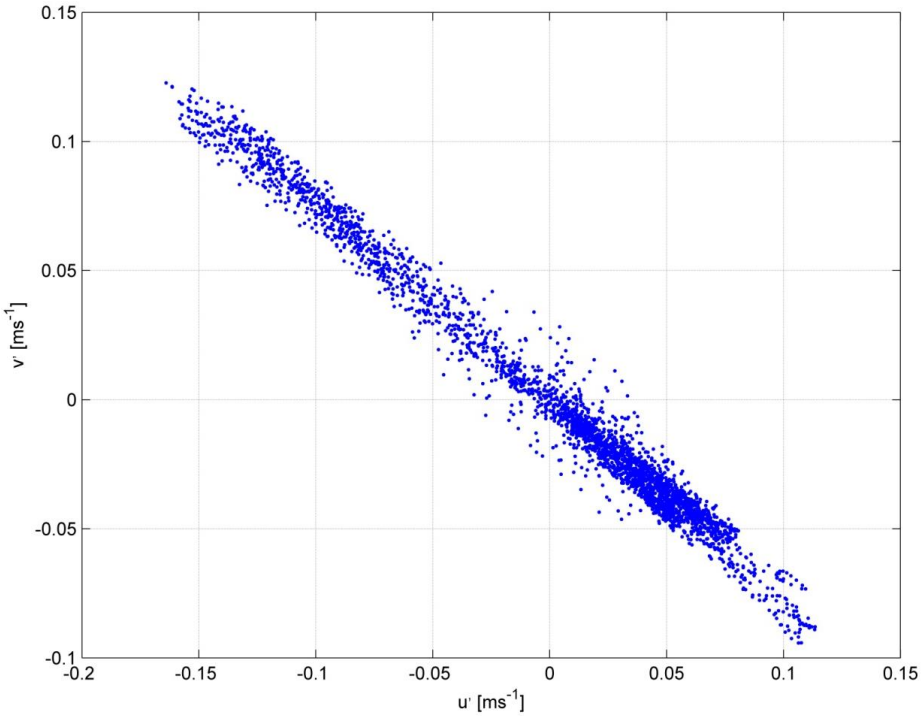

Figure 2.6 Minor and principal axis for cell 19 (1.12 m) at M location.

Table 2.1 Along-channel velocity characteristics at sites S, M and D.

Site	**Subtidal regime**					
	α_{mean}	$\alpha_{pr\ ax}$	$\overline{u_a}$	$\overline{u_m}$		
S	-46.9	-46.0	0.104	0.103		
M	-39.6	-40.6	0.084	0.089		
D	-2.5	-7.5	0.104	0.105		
Tides, amplitude					$\frac{M_2}{\overline{u_m}}$	$\frac{M_4}{M_2}$
K1	M2	S2	M4	M6		
0.011	0.072	0.003	0.035	0.007	0.84	0.49

CHAPTER 3

RESULTS

3.1 OVERTIDES

Tidal amplification in the convergent estuary renders tidal dynamics increasingly non-linear (Seim et al., 2006). Tides become asymmetric and their distortion is related to finite amplitude effects and generates overtides. The ratio of M_4 and M_2 can reveal a tidal distortion in the transition zone. I performed a harmonic analysis using stream flow velocity from USGS. I applied the predominant semidiurnal constituent M_2 and compared what happened when the effect of M_4 and M_6 harmonics (see table 1 and figure 3.1) are added. I found that the M_4 amplitude of along-channel velocity oscillation exceeds 45% of the corresponding M_2 amplitude. This percentage shows evidence that within the transition zone there exist a strong tidal distortion related to abrupt bathymetry changes, convergence of the channel, and an enhanced quadratic bottom friction due to the superposition of fluvial and tidal currents. The harmonic analysis allows for observing the presence of overtides. Thus, the relation between steady and low discharge and the spring and neap tides (Figure 3.1b) is identified. The discharge was fairly uniform through the time period. Specific moments in time for constant and variable discharge are examined to resolve along-channel depth-averaged momentum balance are discussed in section 3.6 (showed in vertical gray bars in figure 3.1b).

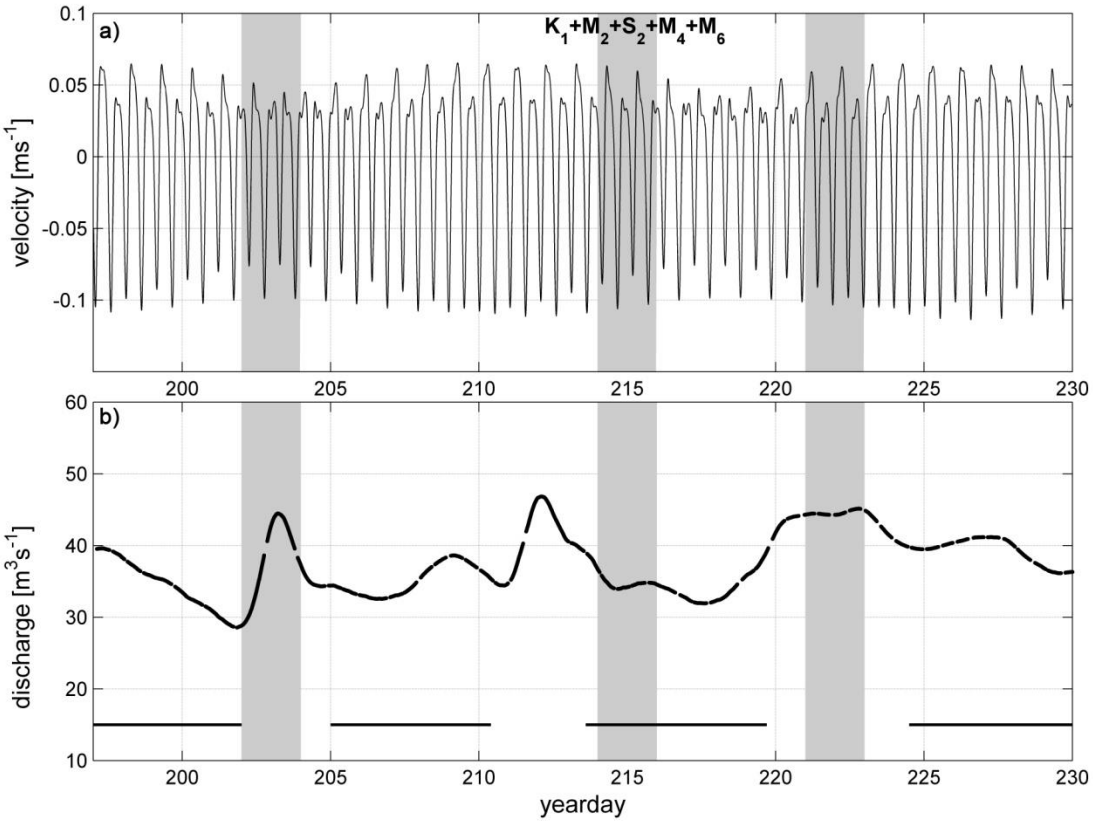

Figure 3.1 (a) Tidal streamflow prediction based on the harmonic analysis of the USGS data: sum of K_1, M_2, S_2, M_4 and M_6 constituents; (b) the Santee River discharge during the 2010 deployment. Vertical gray bars indicate time intervals for the detailed momentum balance analysis in Section 3.6.

Times series of the free surface tidal oscillations were obtained from the bottom pressure records by subtracting a 1-day LPF time series from 1-hour LPF time series. A similar procedure was performed with the along-channel velocity records in order to obtain the along-channel tidal velocity time series. I estimated a time-lagged correlation coefficient between the free surface tidal oscillations and the along-channel tidal velocity for S and M locations using those time series (Figure 3.2b). It was found that the time lag between velocity and free surface at locations S and M is the same (120 min). The correlation is negative due to the tidal wave propagation upstream. Figure 3.2c shows the

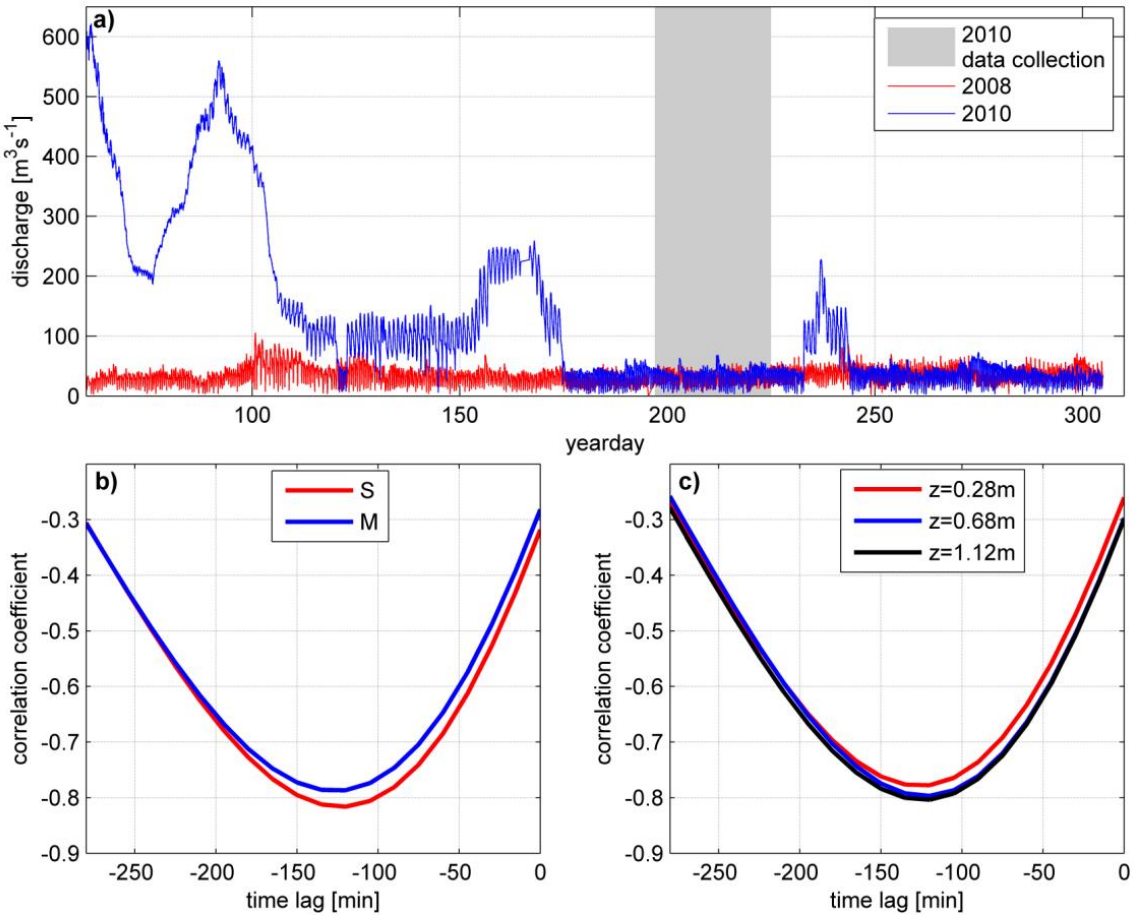

Figure 3.2 (a) The Santee River discharge measured at USGS station in 2008 and 2010, the gray bar represents time interval of the 2010 deployment. Time-lagged correlation coefficient between tidal free surface and along-channel velocity oscillations from (b) locations S and M, depth-averaged velocity; and (c) from near-bottom, middle and top cells at M location, cell 2 (z=0.28 m), cell 10 (z=0.68 m) and cell 19 (z=1.12 m).

lag for the middle location from the bottom, middle and the top cells, which show the same results. The time-lag between the free surface tidal oscillations and the along-channel tidal velocity shows an area of strong bottom friction and convergence of the channel. For the M_2 constituent this time-lag correspond to 58 degrees at the two locations. This phase lag agrees with the strongly convergent and strongly dissipative tidal channel, which is represented by up to a 90 degree phase lag [*Lanzoni and Seminara, 1998*]. During the 2008 deployment (refer to figure 2.2 for location) it was also found significant time lags for the

M_2 constituent in both locations, S (68 degrees) and R (51 degrees). These results showed that the phase difference between water level and the currents velocities decreases moving inshore as the phase decreases from S (2008) to M (2010) and R (2008). These changes in phase result as an effect of bottom friction and channel convergence, which have important implications for the tidal energy carried by tidal waves (Seim et al., 2006). As the phase increases upstream the tidal energy flux decreases.

3.2 ESTIMATING THE ALONG-CHANNEL MOMENTUM BALANCE

The focus of this study is to resolve the depth-averaged along-channel momentum balance in the transition zone. This zone is part of a long channel of fresh water reach, hence a shallow water equation and hydrostatic approximations can be applied, as a result the along-channel momentum balance can be written as,

$$\underset{\boldsymbol{A}}{\frac{\partial u}{\partial t}} + \underset{\boldsymbol{B}}{u\frac{\partial u}{\partial x}} + \underset{\boldsymbol{C}}{v\frac{\partial u}{\partial y}} = \underset{\boldsymbol{D}}{-g\frac{\partial \eta}{\partial x}} - \underset{\boldsymbol{E}}{\frac{\tau_b}{\rho h}} + \underset{\boldsymbol{F}}{\mathcal{F}_x} + \underset{\boldsymbol{G}}{\mathcal{F}_y} \qquad (1).$$

Here u is the depth-averaged along-channel velocity (positive downstream), v is the depth-averaged across-channel velocity, g=9.81 ms^{-2} is the acceleration due to gravity, η is the perturbation of free surface from a horizontal level (positive upward), τ_b is the bottom stress, ρ is the water density and h is the water depth, and $\mathcal{F}_x$ and $\mathcal{F}_y$ represent the horizontal transfer of momentum along x- and y-coordinates. The current measurements were averaged over a 2 min interval. The measurements yield estimates for the following momentum balance terms: ***A*** (inertia or local acceleration), ***B*** (along-channel advective acceleration), ***D*** (along-channel pressure gradient force), and ***E*** (bottom friction) at location M. Figure 2.3 shows strong along-channel water depth variations and it has been shown by Basdurak and Valle-Levinson (2012) that the advective acceleration can be of the same

magnitude as the leading term in estuarine tributaries. For the purpose of subsequent discussion, I define the dissipative term *Diss* as $Diss=\boldsymbol{A}+\boldsymbol{B}-\boldsymbol{D}$, and the residual term $\boldsymbol{R}=\boldsymbol{A}+\boldsymbol{B}-\boldsymbol{D}-\boldsymbol{E}$. This *Diss* term then enclose ***C***, ***E***, ***F*** and ***G*** terms.

3.3 DEPTH-AVERAGED VELOCITY AND ACCELERATION TERM

As a first step, I estimated the depth-averaged along-channel velocity at each site of measurements. For the AWAC data, due to their coarse vertical resolution and shallow water at site S, I simply averaged the velocities from cells 1 and 2. This yielded the record-mean depth-averaged along-channel velocity of 0.103 ms^{-1}. In the case of M location I used two different approaches. The first approach applied was to calculate depth-averaged along-channel velocity for M and D locations. I used the time-averaged along-channel velocity profiles to find the depth corresponding to the depth-averaged velocity. At locations M and D, where HR and LR Aquadopps were deployed, respectively, only the lower portion of the water column was sampled, which necessitated an extrapolation of the velocity profile to the surface. I assumed a logarithmic function of velocity distribution with depth, and used a linear regression (least squares fit) to extrapolate velocity values as a function of ln *z* (Figure 3.3). Once the full record-mean along-channel velocity profile was reconstructed, I found a depth-averaged velocity value and its corresponding depth. I found that for the HR Aquadopp, the record-mean depth-averaged velocity was 0.086 ms^{-1}. Due to the depth of this velocity being above the range of the HR Aquadopp sampling, I converted a low-pass filtered velocity series at cell 19 (1.12m), location M, into the depth-averaged series by applying a coefficient of 1.03. This coefficient is a ratio of the depth-averaged and the cell 19 along-channel record-mean velocities. For the LR Aquadopp, the

depth-averaged velocity, 0.105 ms^{-1}, corresponded to the velocity at cell 16 (1.92 m). Hence, this cell was used as a proxy for the depth-averaged velocity at site D.

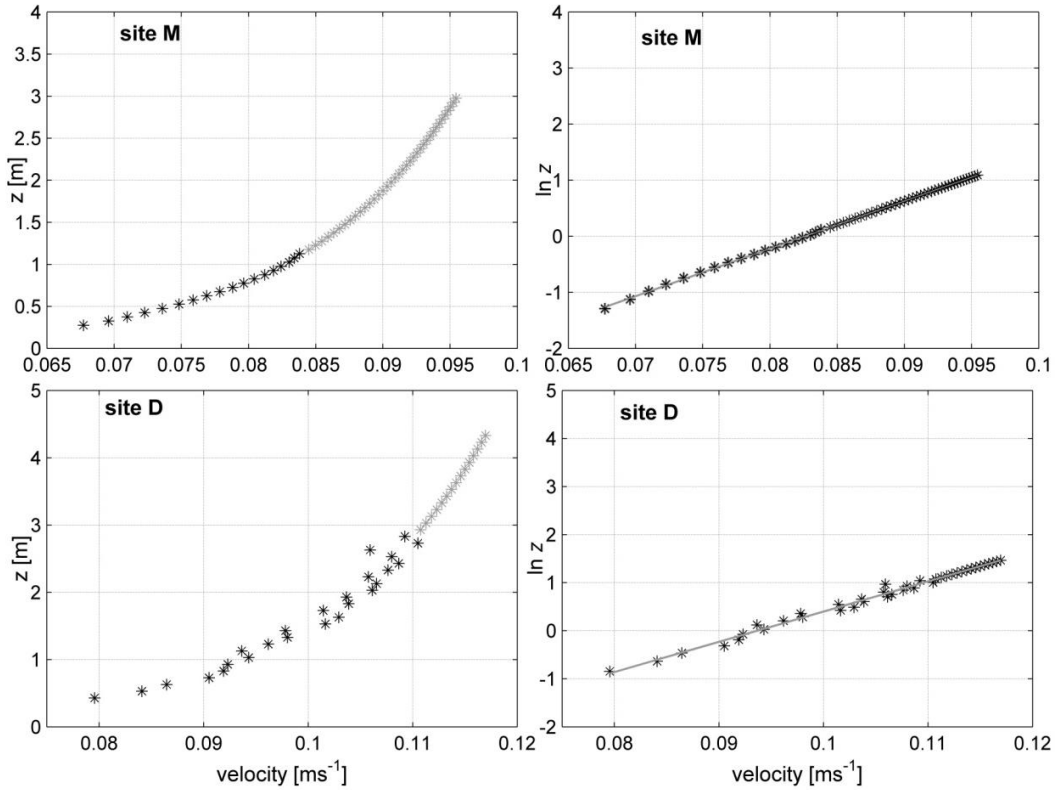

Figure 3.3 Extrapolation of record-mean along-channel velocity profiles to the surface at sites M (top) and D (bottom). The extrapolated values are shown as gray asterisks on left panels.

The second approach to obtain a depth-averaged along-channel velocity at M location was to linearly extrapolate measured velocity profile to the surface using 5 uppermost cells and applying a least-squares fit. Using this approach yields to a record-mean along-channel velocity of 0.089 ms^{-1}. This result is comparable to the result obtained using the first approach. Data from location D (LR Aquadopp) proved to be too noisy for extrapolating them to the surface and obtaining their depth-averaged estimates using the

second approach. Figure 3.4 shows the depth-averaged velocity time series at location M using the first and second approaches as well as the depth-averaged velocity for S location.

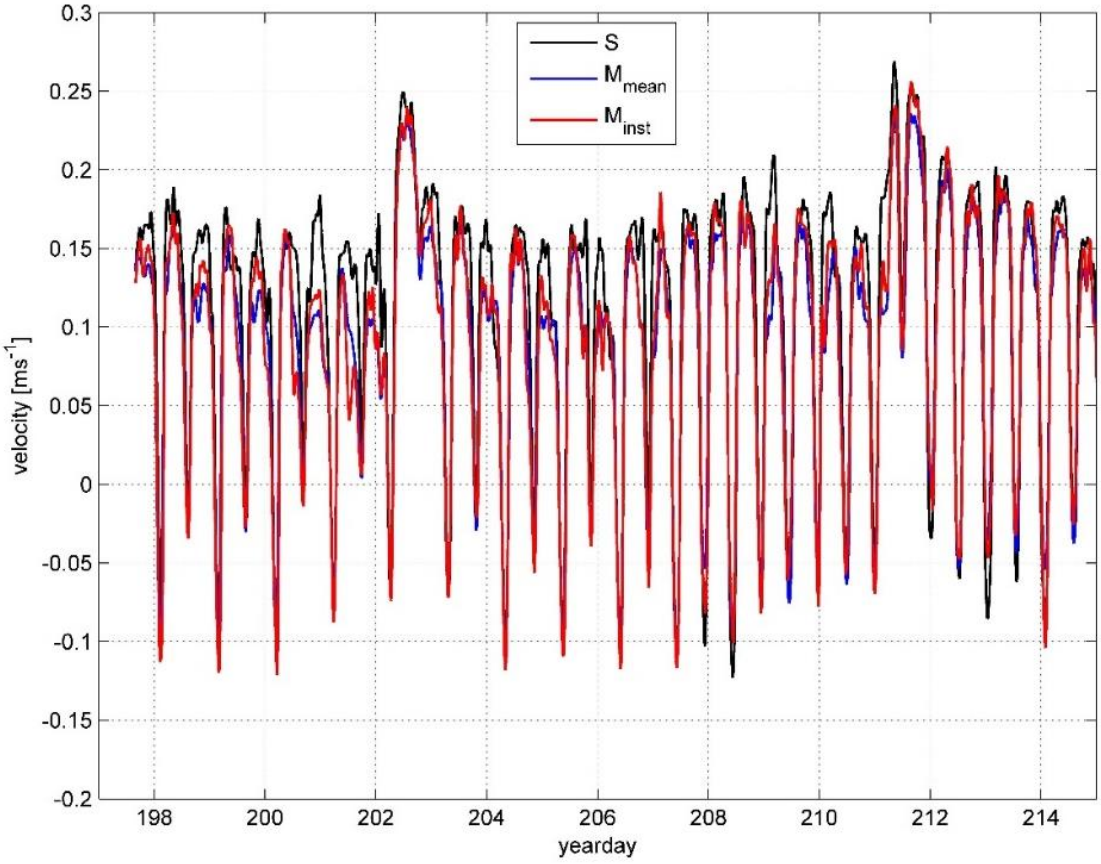

Figure 3.4 Depth-averaged velocity time series for S, M_{mean} (first approach) and M_{inst} (second approach) locations.

It is interesting to note that while the depth increases from S to D locations, the depth-averaged velocity does not decrease. The record-mean discharges through the unit cross-channel distance at S, M, and D sites are 0.24, 0.26, and 0.45 m^2s^{-1}, respectively. Since the net discharge integrated across the channel should be conserved, this discrepancy implies that the transverse structure of the along-channel flow changes from site to site (see figure 2.3 for reference). Using cross-sectional areas presented in figure 2.4 and the mean

depth-averaged velocities for S = 0.103 ms^{-1}, M = 0.089 ms^{-1} and D = 0.105 ms^{-1} discharge values for S, M and D are 18.60, 14.53, 20.0 m^3s^{-1}, respectively. These last values also support the change in the transverse structure.

I utilized the second approach, for location M, to obtain the depth-averaged velocity time series and used this to estimated term ***A*** by approximating a time derivative with central differences. I selected this approach because it accounts for the fluctuations of water level that correspond to each velocity profile.

3.4 ALONG-CHANNEL ADVECTICE ACCELERATION TERM

Once the depth-averaged velocity time series are obtained for each location, I estimated term ***B*** using three difference finite difference approximations. In the presence of non-linear waves the advection terms (***B***) needs to be taken into account, especially because of strong bathymetric variations. The advective acceleration term was calculated using three different numerical schemes: central difference (whole study site), forward difference (deep part of the study site) and backward difference (shallow part of the study site). For the central difference approximation, I subtracted data at location S from data at location D: D-S; the forward/backward differences were approximated as D-M and M-S, respectively (figure 3.5). These approaches were done to help to understand that while the depth increases from S to D locations, the depth-averaged velocity does not decrease. Furthermore, the advective acceleration term requires a small spatial scale because there is a relation between spatial distributions with respect to along-channel flow, and understanding its effect among the three locations may be beneficial.

Figure 3.5 showed the advective acceleration numerical schemes, and the deeper part of the study site (forward difference) and the shallower part (backward difference)

showed different signs most of the time. A possible explanation for this phenomenon is the redistribution of cross-channel momentum as a result of a convergence at the central location from the forward to the backward differences. Measurements at location D were proven to be too noisy; as a consequence, hereafter for the estimation of the depth-averaged along-channel momentum balance I selected the backward difference.

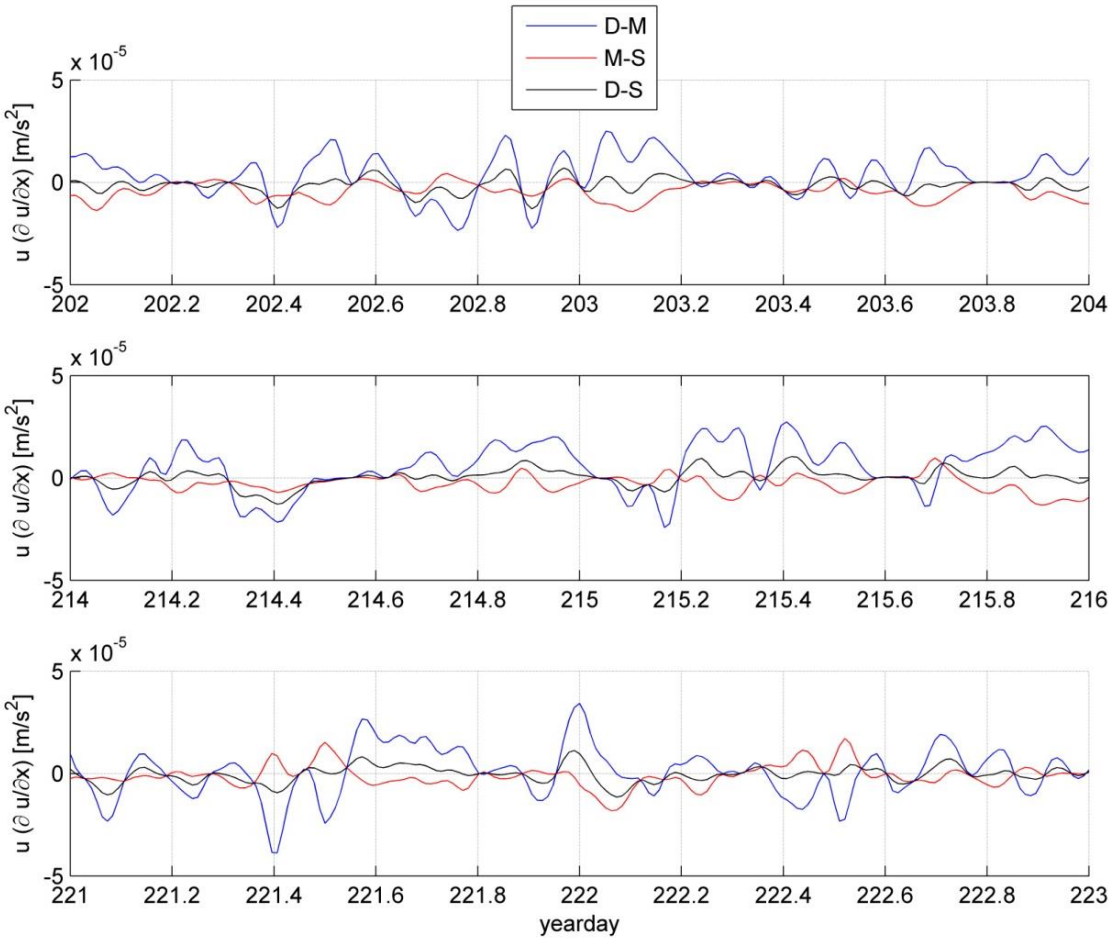

Figure 3.5 The advective acceleration terms using three different approximations: central (D-S), forward (D-M) and backward (M-S) differences.

3.5 BOTTOM FRICTION

In the study of convergent estuaries, bottom friction plays an important role in the hydrodynamics. Currents at site M are in good alignment for logarithmic velocity profile (Figure 2.5). The bottom friction term was estimated from the logarithmic boundary layer approximation [*Schilighting*, 1960]. The velocity distribution law by *Prandtl* is defined by

$$u(z) = \frac{u_*}{k} \ln\left(\frac{z}{z_0}\right) \qquad (2),$$

$$\text{where} \quad u_* = \sqrt{\frac{|\tau|}{\rho}} \qquad (3).$$

Here z is the height above the bottom, u_* is the friction velocity, z_0 is the roughness height, k=0.41 is the Von Kàrmán's constant, and τ is the turbulent shear stress. Using equation (2) and (3) the along-channel bottom stress τ_b and the drag coefficient C_d is defined, by

$$\tau_b = \rho C_d u_r |\vec{v}_r| \qquad (4)$$

$$C_d = \left(\frac{k}{\ln\left(\frac{z}{z_0}\right)}\right)^2 \qquad (5).$$

Here $\vec{v}$ is the horizontal velocity vector, index *r* refers to the depth-dependent velocity at the reference level *z*, and the drag coefficient depends on the choice of *z*. The drag coefficient, and consequently the bottom stress, was estimated only for those velocity profiles which satisfied the following screening criteria (same as in Yankovsky et al., 2012): change of the horizontal velocity direction with depth did not exceed 10^o, and

$|\partial u_a / \partial t| \leq 10^{-6}$ ms^{-2}. These two criteria are used because Prandtl's theory assumes steady-state, parallel flow. Hence, the bottom boundary layer (BBL) current representing flood and ebb conditions using cell 2 (z=0.27m) through cell 7 (z=0.52m). Figure 3.6 shows examples of the logarithmic velocity profiles during ebb and flood conditions. I did not use the full range of the measured velocity profile because in some cases the upper part of the profile departs from its logarithmic structure; typically this happens during ebb (figure 3.6c). The deviation of velocity profile from the logarithmic structure is likely to cause variations in the estimation of the C_d. However, the quality of the data fit to a logarithmic profile for all the screening data show a R^2 of 0.97 for cells 2 through 7 and R^2 of 0.93 for the whole range (cells 2 through 19).

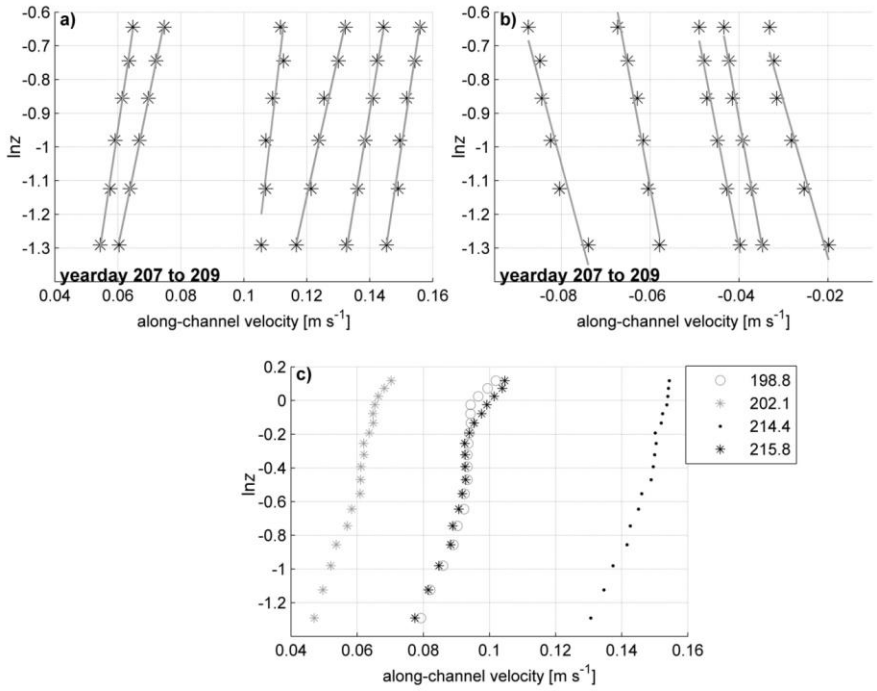

Figure 3.6 Site M, examples of logarithmic velocity profiles, bin 2 through 7 (top), ebb (a) and flood (b) conditions for yearday 207 through 209. Black asterisks are the velocity measurements (cell 2 through cell 7) and gray lines are the least-squares linear fit; (c) examples of velocity profiles departing from their logarithmic structure in the upper part.

Bottom drag estimates are shown in Figure 3.7 as a function of the along-channel velocity corresponding to z=0.52 m (cell 7) for ebb and flood conditions separately. C_d values show a tendency to change with the velocity magnitude. Due to this tendency, C_d values were averaged for the along-channel velocity bins separated by 0.02 ms^{-1} intervals and the corresponding 95% confidence limits for these averaged C_d were estimated. Figure 3.7 also shows bottom drag coefficients estimated in 2008 the deployment (presented in Yankovsky et al., 2012). These bottom drag coefficients show the following features: (i) the C_d tends to decrease with an increase in velocity magnitude and this tendency is more evident in 2010 data; (ii) there is an asymmetry in the bottom drag between ebb and flood conditions, with higher C_d coefficients during flood. Averaged C_d values for flood conditions are 0.018 (2008) and 0.011(2010), while for ebb they are 0.011 (2008) and 0.0046 (2010). Previous studies in estuaries and in tidal rivers (e.g., Scully and Friedrichs, 2007; Fong et al., 2009) provided observational examples of asymmetry in the bottom drag.

While bottom roughness and bottom drag characterize local flow conditions and can exhibit strong spatial variations, I argue that lower bottom drag in 2010 existed in the entire study area. Indeed, different bottom roughness was likely preconditioned by different flow regimes in 2008 vs. 2010 prior to instrument deployments (Figure 3.2a). In 2008, low discharge conditions existed for several months before the deployment, while in 2010 the river discharge varied between high and medium values before the deployment. Higher discharge results in a unidirectional, fluvial-dominant flow regime with a stronger bottom shear stress due to higher flow velocities. Obviously, the impact of this higher discharge on bed forms lasted for some time even after the discharge had subsided.

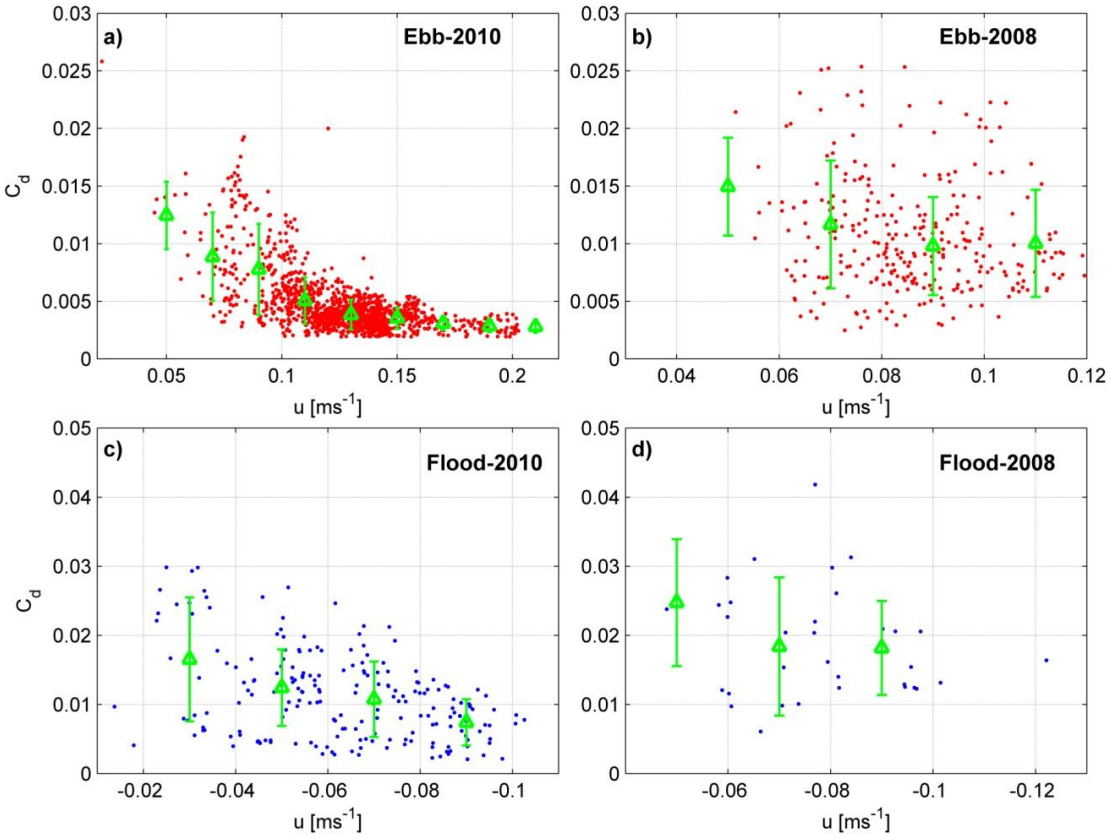

Figure 3.7 Drag coefficient versus along-channel velocity measured at cell 7 (z=0.52m) at M site: (a) 2010 deployment, ebb currents; (b) 2008 deployment ebb currents; (c) 2010 deployment, flood currents; (d) 2008 deployment, flood currents. Green triangles are drag coefficients averaged over 0.02 ms^{-1} velocity intervals, and vertical bars are their corresponding 95% confidence intervals.

3.6 ALONG-CHANNEL PRESSURE GRADIENT FORCE

The pressure gradient force term ***D*** can be expressed as:

$$-g\frac{\partial \eta}{\partial x} = -g\left(\frac{\partial \overline{\eta}}{\partial x} + \frac{\partial \eta'}{\partial x}\right) \qquad (6).$$

Here the overbar and prime symbols refer to the record-mean and perturbed values, respectively. The perturbed pressure gradient force was obtained from the SBE 26plus at locations D and S. In order to obtain the actual value of the pressure gradient force, the record-mean pressure gradient has to be added (which is unknown). Assuming that the

time-averaged pressure gradient is balanced by bottom friction, $-g\frac{\partial\overline{\eta}}{\partial x}-\frac{\tau_b}{\rho h}=0$, the averaged along-channel velocity u_r and water depth at M location is used to find the mean pressure gradient force value $-g\frac{\partial\overline{\eta}}{\partial x}=\frac{C_d\overline{u_r^2}}{\overline{h}}$. For the record-mean pressure gradient estimate, I chose the drag coefficient from the bin containing the record-mean velocity in cell 7. The corresponding C_d (ebb conditions) is 8.9×10^{-3} and u_r=0.075 ms^{-1} which yields a mean pressure gradient force of 1.66×10^{-5} ms^{-2}.

The estimate for $-g\frac{\partial\overline{\eta}}{\partial x}$ can be further verified using an alternative approach based on the linear regression between the perturbed pressure gradient force and the sum of other momentum balance terms. The shift of the regression line relative to the origin will thus account for the missing record-mean part of the pressure gradient force (6). Figure 3.8 shows two plots: ***A***+***B***-***E*** and ***A***-***E*** versus pressure gradient force. I found for ***A***+***B***-***E*** the linear regression shift is 1.84×10^{-5} ms^{-2}, while for ***A***-***E*** combination (two other leading momentum balance terms are compared with the pressure gradient), this shift is 1.52×10^{-5}ms^{-2}. That is, the estimate for the record-mean pressure gradient force based on the dynamical consideration is within the range set by linear regression fits. This verification illustrates that the pressure gradient force is properly represented in the along-channel momentum balance.

3.7 MOMENTUM BALANCE

The estimate of the along-channel depth-averaged momentum balance at the center of the study area (site M) is summarized in Figure 3.9. I estimated the pressure gradient term of the momentum balance (1) at the central location M, approximating partial derivatives with central finite differences, whereas the advective acceleration was estimated using the backward difference. For reference, Figure 3.9a shows the free surface

oscillations and the depth-averaged velocity at location M, where flood and ebb currents are short-lasting and long-lasting, respectively. Both the pressure gradient force and local acceleration are of the leading order, while the advective acceleration (based on backward difference) is relatively small (Figure 3.9b). I assumed that bottom friction plays a leading role in tidal dissipation so that the dissipative term *Diss* should be comparable with the bottom friction term ***E*** if the momentum balance terms are properly resolved. Figure 3.9c captures this feature and shows an overall good alignment between *Diss* and ***E***.

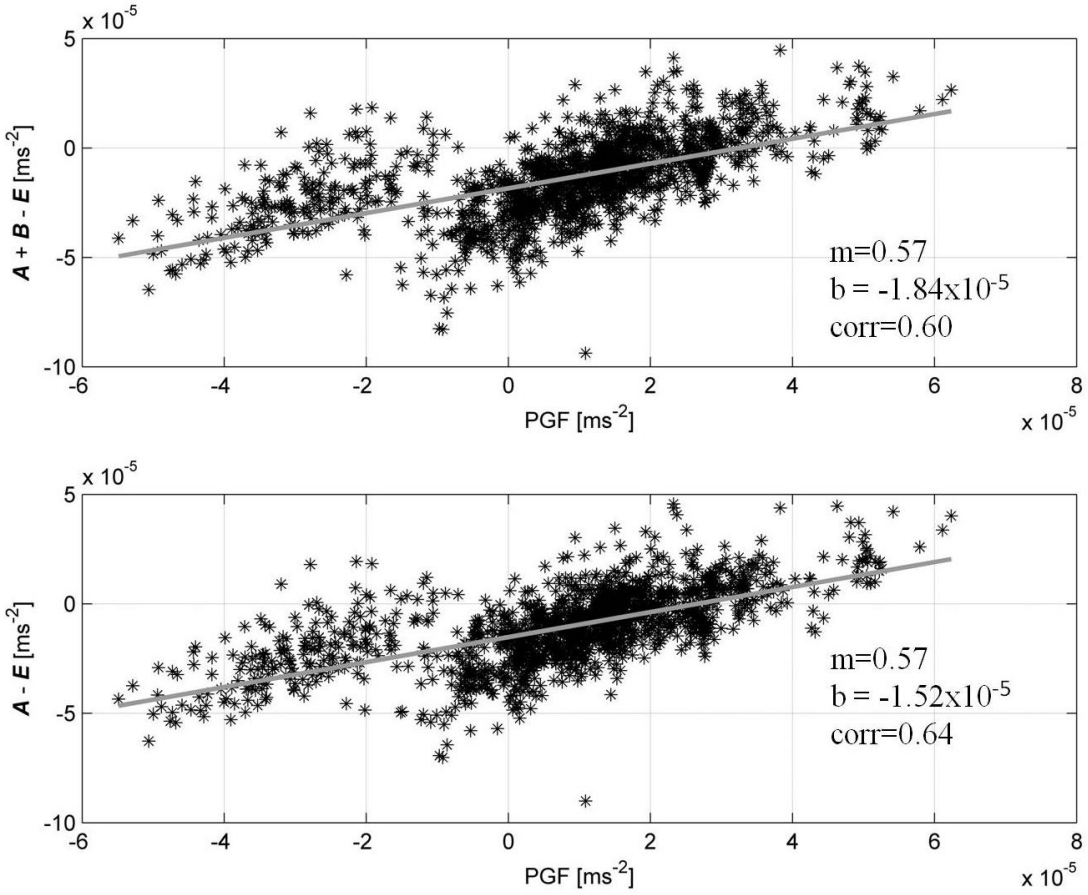

Figure 3.8 Regression line between ***A***+***B***-***E*** and ***A***-***E*** terms with respect to PGF.

The relationship between *Diss* and ***E*** terms is quantified in Figure 3.10a: the correlation between the two terms is 0.69, while the linear regression slope is 0.54. Since

the slope of the regression line is less than 1, I infer that the bottom friction underestimates on average the dissipative term, which suggests that the bottom friction is not the only term responsible for the momentum dissipation. The other likely candidates are the momentum balance terms ***C*** and ***G*** in (1), this feature, especially the possible contribution of the ***G*** term, is explained in more detail in the appendix.

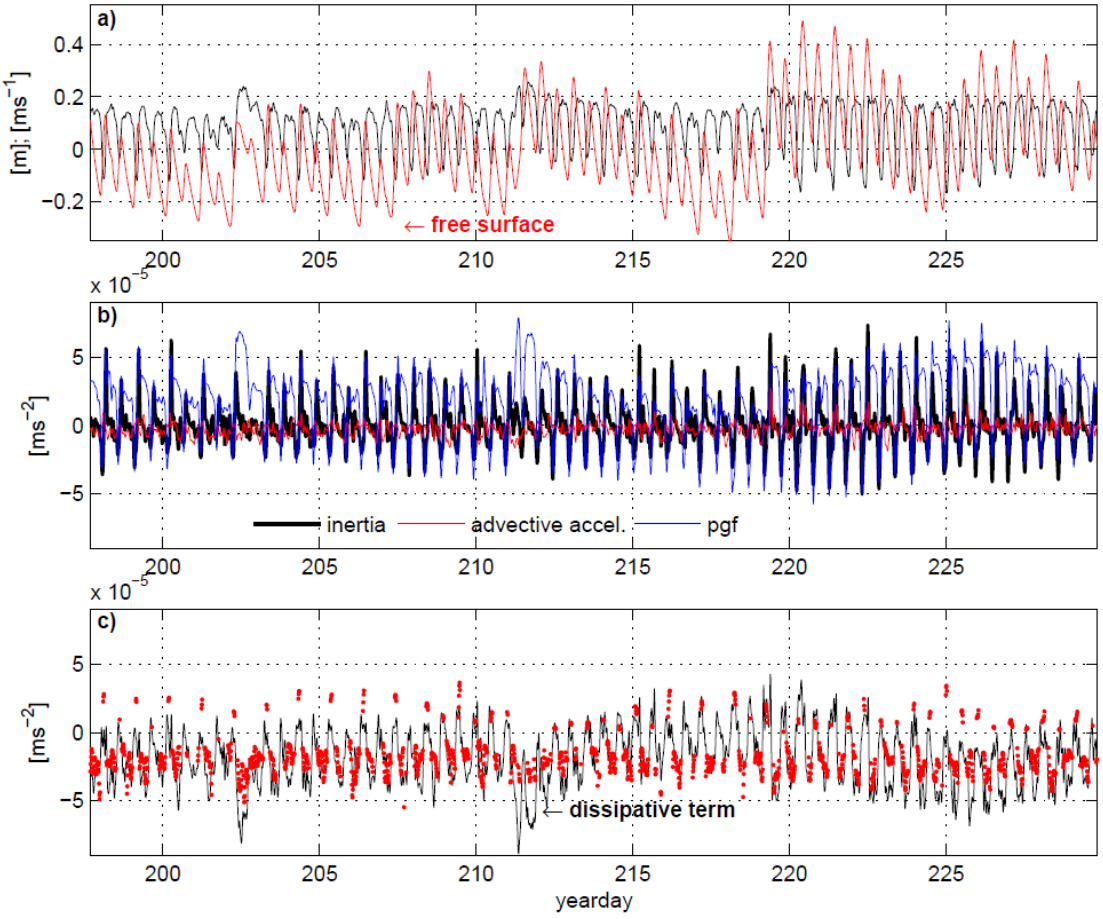

Figure 3.9 Momentum balance term estimates for the entire record**:** (a) free surface and depth-averaged along-channel velocity at site M; (b) inertia (black), advective acceleration (red) and pressure gradient force (blue); (c) dissipative (black) and bottom friction (red dots) terms.

Now three subsets of the momentum balance analysis (marked by gray vertical bars in Figure 3.1b) are considered: two time intervals corresponding to steady discharge

conditions when the momentum balance was particularly well resolved and a time interval with variable river discharge. The steady-state river discharge conditions are presented in Figure 3.11 (yearday 214 through 216) and Figure 3.12 (yearday 221 through 223). Figures 3.11b, 3.11c, 3.12b and 3.12c show that the along-channel momentum balance is resolved, i.e., *Diss* and ***E*** terms are comparable, although during ebb the bottom friction underestimates the dissipative term most of the time. The principal balance during flood is between the pressure gradient force and the inertia terms, as in the case of long gravity waves. However during ebb, the balance is between the pressure gradient force and the bottom friction terms, as in the case of steady-state current. Surprisingly, the contribution of advective acceleration remains small most of the time, even though the study area is characterized by strong along-channel bathymetric variations.

The momentum balance in Figure 3.13 is similar to previous figures, except for the period yearday 202.3 through 202.7, when the river discharge and the downstream velocity both increase. This happens as well during yearday 212 (Figure 3.1 shows discharge peaks for those yearday). During these time intervals, the along-channel pressure gradient force becomes particularly high and the absolute value of the dissipative term exceeds the bottom friction by a factor of 2 or 3. This result shows that river discharge plays an important role in the depth-averaged current velocity and free surface variations. For example, around yearday 202.7 the fluvial flow increases and there is almost no flow reversal. As the fluvial flow increases there is a subsequently enhanced pressure gradient force causing the flow to accelerate up to a certain threshold. As a consequence, the pressure gradient force is not balanced by inertia and bottom friction, but instead this instability threshold is reached and

a lateral eddy is developed. Appendix A shows a more detail explanation and an estimation of the eddy viscosity.

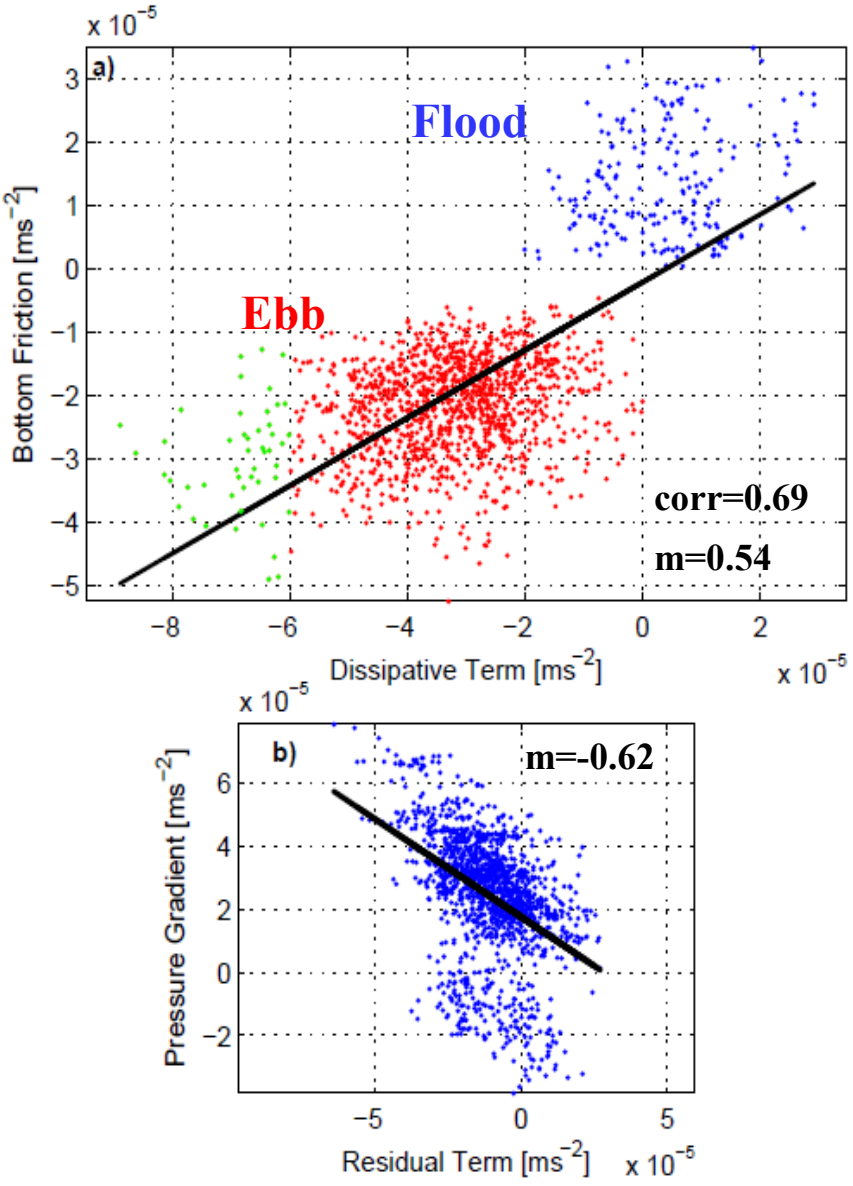

Figure 3.10 Scatterplot of (a) bottom friction versus dissipative terms (flood is in blue, ebb is in red, and ebb with large absolute value of the residual term is in green, corr is the correlation coefficient, and (b) pressure gradient versus residual ***R*** terms. In both panels, solid line is the linear regression and m is its slope.

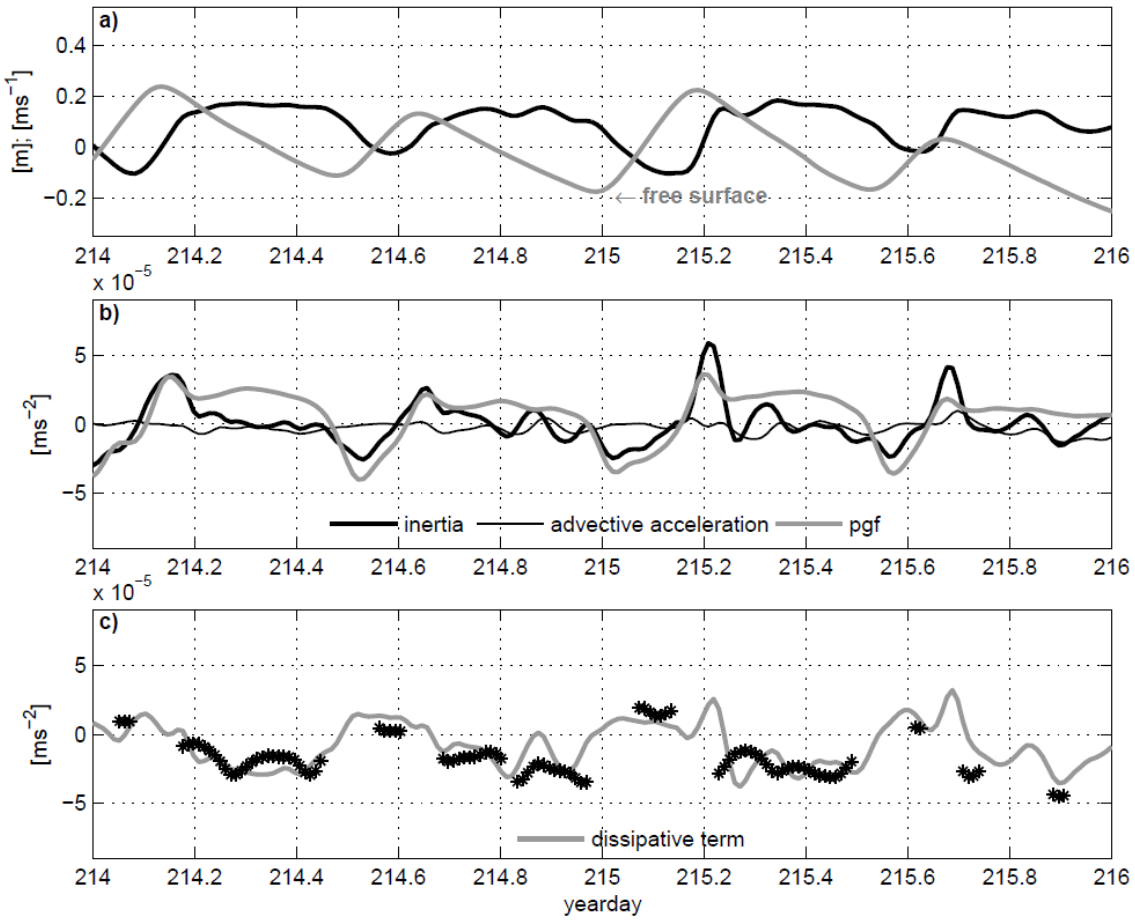

Figure 3.11 Momentum balance term estimates for yearday 214-216**:** (a) free surface and depth-averaged along-channel velocity at site M; (b) inertia (thick black), advective acceleration (black) and pressure gradient force (gray); (c) dissipative (gray) and bottom friction (black star) terms.

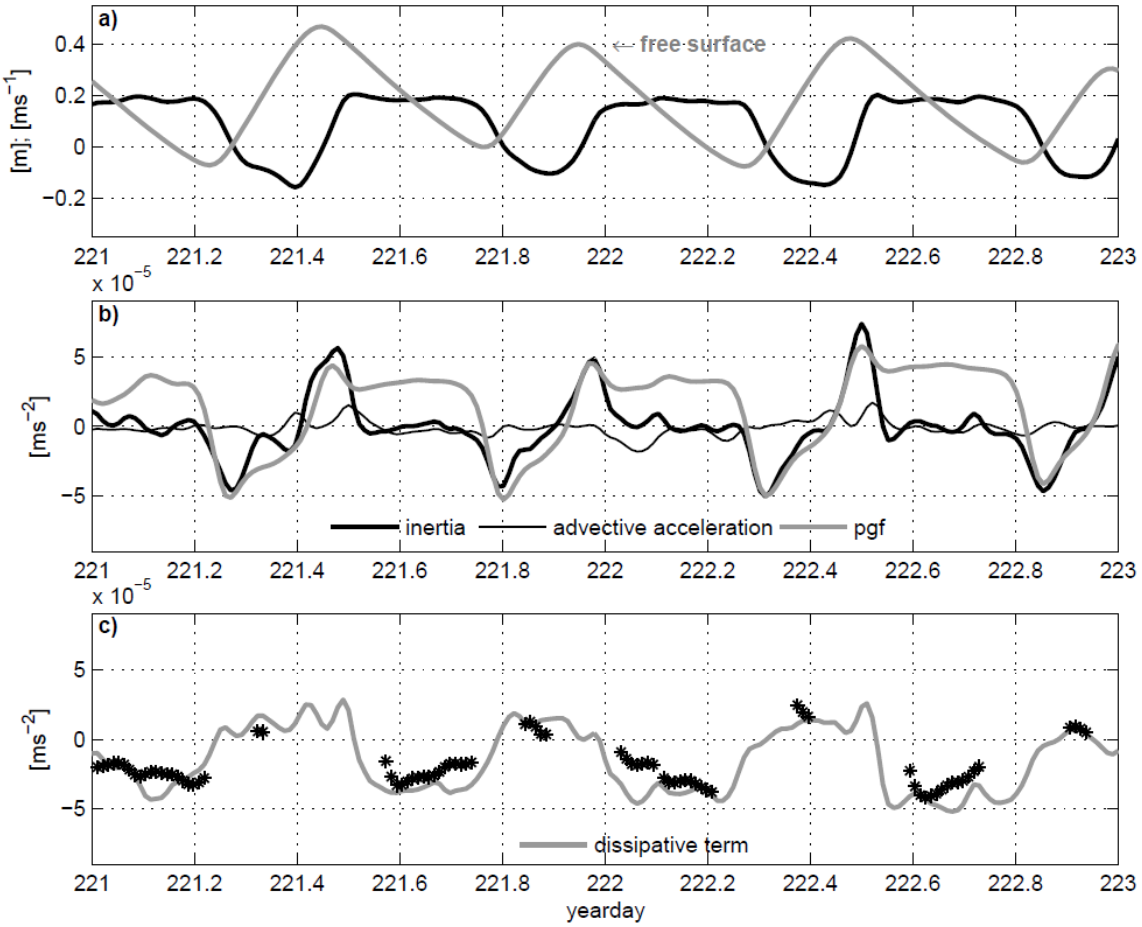

Figure 3.12 Momentum balance term estimates for yearday 221-223**:** (a) free surface and depth-averaged along-channel velocity at site M; (b) inertia (thick black), advective acceleration (black) and pressure gradient force (gray); (c) dissipative (gray) and bottom friction (black star) terms.

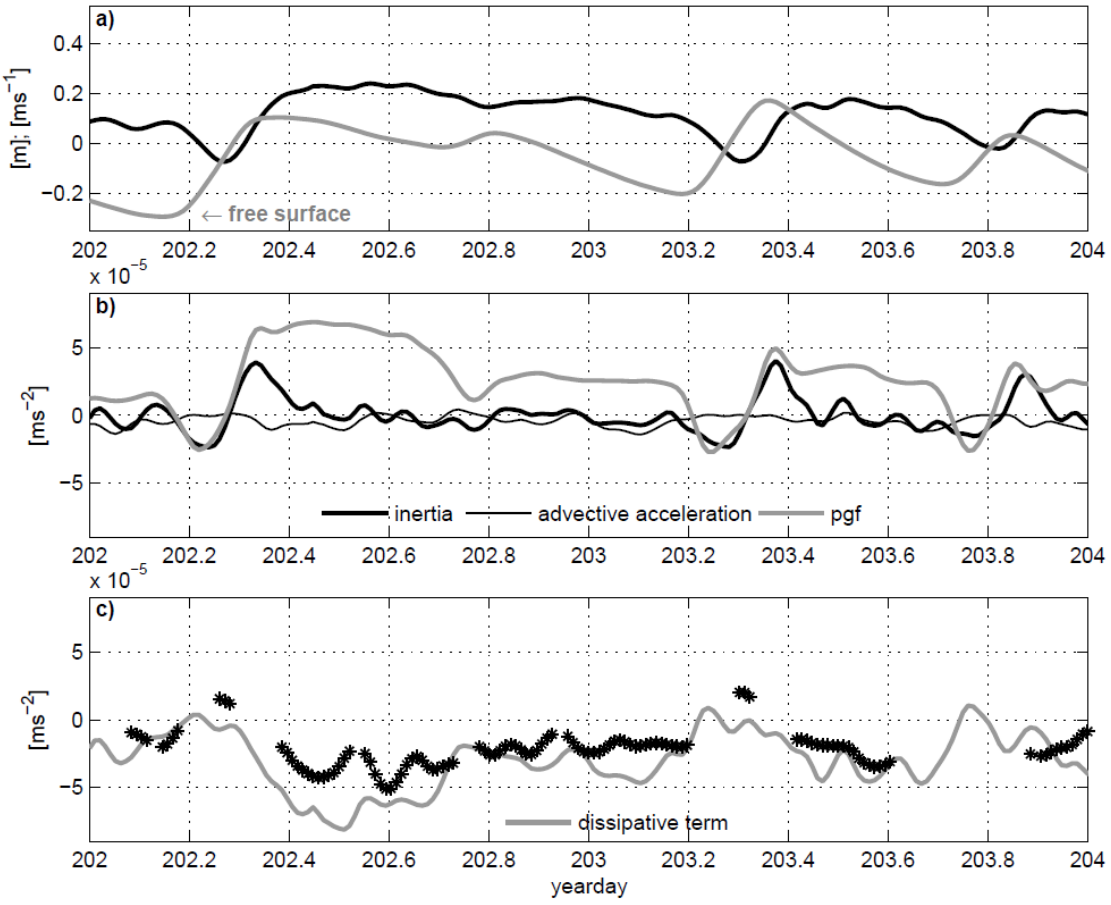

Figure 3.13 Momentum balance term estimates for yearday 202-204**:** (a) free surface and depth-averaged along-channel velocity at site M; (b) inertia (thick black), advective acceleration (black) and pressure gradient force (gray); (c) dissipative (gray) and bottom friction (black star) terms.

3.8 Accuracy of the Pressure Gradient Force Term

It is widely accepted that the pressure gradient force (***D***) it is of the leading terms in the along-channel momentum balance. Figures 3.12b, 3.12c, 3.13b and 3.13c show that the along-channel momentum balance terms, were *Diss* and ***E*** terms are comparable for the most part. Undulations in the pressure gradient force appeared after yearday 223 and as result there is an increase in misalignment between *Diss* and ***E***. This undulation is most likely to carry a discrepancy when calculating the *Diss* term. There are two possible

explanations to this phenomenon, (1) instrumentation or (2) it is natural occurring. Figure 3.14 shows a plot of the pressure gradient force term (***D***) and the pressure gradient force calculated taking gauge station measurements from USGS gauging station 02171905 (gage datum = -19.55 feet above NGVD29), located 10 km from the mouth and from USGS gauging station 02171700 1 km upstream from the study site hereafter, "ocean-river". This ocean-river pressure gradient force (black line in figure 3.14) is compared with the pressure gradient force term ***D*** (red line in figure 3.14) described in section 3.6. These two pressure gradient are base on different spatial scale and are not expected to coincide, but on subtidal frequencies they show a similar trend. Figure 3.14 shows that after approximately yearday 223 there is an opposite behavior between pressure gradient forces (one increase, while the other decrease). I decided to plot the pitch and roll during that period of time for location S to seek a better understanding.

I plotted the pitch and roll for the AWAC instrument located along-side with the SBE 26plus (location S), which was used to calculate pressure gradient force. I found a change in the pitch and roll at approximately yearday 223 (Figure 3.15). I hypothesized that the movement of instrument due to the accumulation of sediments could contribute to the undulation in the pressure gradient force after yearday 223. However, during the first 14 days of the series I inferred that the pressure gradient force is well aligned with the inertia and the bottom friction.

Figure 3.14 Pressure gradient force term ***D*** (red) and pressure gradient force between USGS gauging station 02171905 and USGS gauging station 02171700 (ocean-river). Blue bar shows yearday corresponding to discrepancy between both.

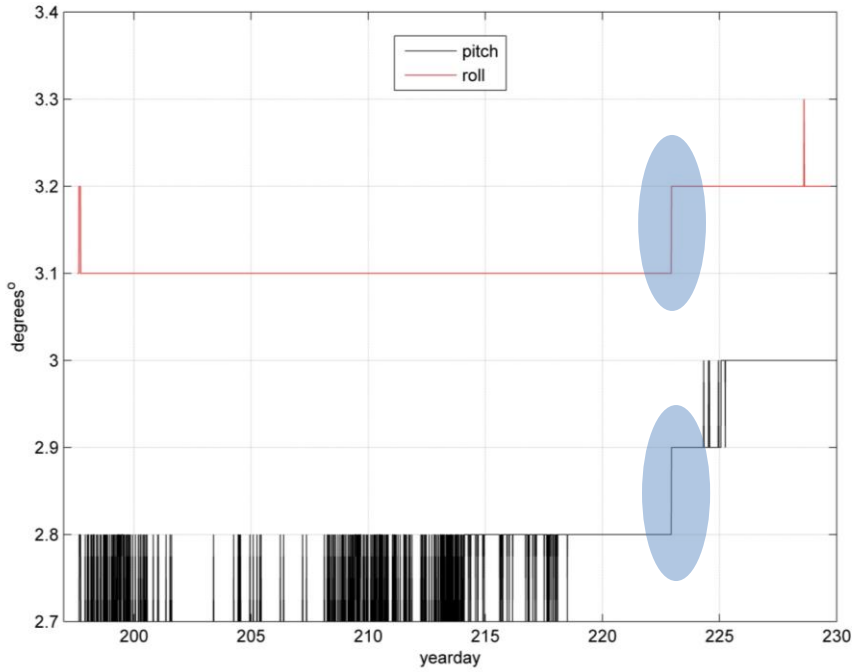

Figure 3.15 Pitch and roll for AWAC, S Location. Blue ovals show discrepancy at yearday 223.

CHAPTER 4

DISCUSSION AND CONCLUSIONS

I analyzed velocity profiles with corresponding bottom pressure records obtained from three different locations (S, M and D) in the reach of the Santee River at the transition zone where the tidal flux and river discharge become comparable. Instruments were deployed in the convergent (with respect to tidal wave propagation) river channel where the nonlinear dynamics was expected to be well pronounced. Using depth-averaged along-channel velocity and pressure records I estimated local and advective accelerations, a pressure gradient force, and a bottom friction based on the logarithmic layer approximation. Using the USGS stream flow and discharge data I performed a harmonic analysis and determined that the study site is characterized by strong tidal distortion associated with the presence of M_4 and M_6 constituents, which proves nonlinear tidal dynamics. I found the time-lag between the free surface tidal oscillations and the along-channel tidal velocity for S and M locations. This time-lag is the same for both locations and does not vary with depth, which indicates rapid frictional adjustment in the vertical.

This study accounts for strong bathymetric variations, finite amplitude effects and bottom friction in the presence of low river discharge. Under such discharge conditions, the study site represents a transition zone from fluvial to tidal regime, where the river and tidal current velocities become comparable [*Yankovsky et al*., 2012]. During high discharge conditions the flow regime in the study area becomes predominantly fluvial (that is, unidirectional flow, although tidal oscillations are still present).

I resolved, for the most part, the depth-averaged along-channel momentum balance throughout the entire period of measurement. The residual term is consistently smaller than the leading-order momentum balance terms: the pressure gradient force, the local acceleration (inertia), and the bottom friction. Surprisingly, the advective acceleration term is small, although the tidal dynamics clearly shows nonlinearity and the channel depth exhibits more than a two-fold change within the study area. The importance of the momentum "diffusion" is evident in that the record-mean velocity close to the center of the channel does not follow depth variations between the measurement sites but remains fairly unchanged in the along-channel direction. This implies variations in the mean flow transverse structure and hence the lateral momentum redistribution.

I found that the correlation coefficient between bottom friction and the dissipative term is 0.69 with a linear regression slope of 0.54. Since the slope of the regression line is less than 1, I inferred that the bottom friction term underestimates on average the dissipative term, which suggests that the bottom friction is not the only mechanism influencing tidal dissipation. I hypothesize that the discrepancy between the dissipative term and bottom friction is primarily due to lateral eddy viscosity. Based on the correlation between the residual term and the pressure gradient force, I infer that the generation of eddies and the resulting lateral momentum "diffusion" can be triggered by the enhanced along-channel pressure gradient, for instance, when the river discharge abruptly increases (Figure 3.13). Such an enhanced forcing causes the flow to accelerate only up to a certain magnitude, when the instability threshold is reached and the jet structure starts disintegrating into eddies. The presence of bed forms and bathymetric variations in the study area is likely to further amplify the "eddying" of the mean current; the influence of

local bathymetry on the horizontal momentum "diffusion"; and ultimately on tidal dissipation.

I found that there is a change in scattering of the C_d values in relation to the along-channel velocity (Figure 3.7a). The drag coefficient values scatter when velocity is low and, conversely, cluster when velocity is high. This result indicates that for small velocities the uncertainty of the bottom friction estimate will increase. However, these small velocities do not induce strong bottom friction and the leading terms in the along-channel momentum balance are the inertia and the pressure gradient forces. In contrast, for larger velocities when bottom friction is significant, the uncertainty decreases. Thus, the bottom friction and dissipative term comparison is not strongly affected by the uncertainty of bottom drag estimate. Also, the bottom drag coefficient varied between the 2008 and 2010 deployments. This difference can be related with very different river discharge conditions prior to deployments in those years. In particular, medium-to-high discharge in 2010 resulted in stronger, unidirectional currents and higher bottom shear stress, so that the bed forms and bottom roughness could also be affected. The smoother channel conditions existed for some time even after the discharge had subsided by the time of deployment, and were captured by the measurements. Thus, variations in river discharge not only shift the location of the transition zone along the river channel, but can also affect the bottom drag and the efficiency of tidal dissipation.

Few important uncertainties or sources of error of the data analysis which might interfere with the agreement between the dissipative term and the bottom friction are: (1) the presence of scattering in the velocity profiles when I performed the logarithmic layer approximation may have affected the estimate of z_o. (2) The estimation of the spatial

derivative, where the advective acceleration term requires a small spatial scale to be most accurate, whereas the pressure gradient estimation requires a larger spatial scale. (3) The contribution of the lateral momentum terms, ***C***, ***F*** and ***G***. However, I assumed that the lateral momentum term ***C*** (across-channel advective acceleration) might be insignificant because the across-channel pressure gradient, which controls the *v* component, is set by long gravity waves propagating across the channel. The channel width in the area of measurement is 100-130 m under low discharge conditions observed during deployment, and the long wave crosses the channel in less than 40 s (this is an estimation assuming an average water depth of 1 m). As a consequence the lateral momentum term ***C*** is associated with time scale shorter than the averaged internal, over a 2 min interval, of the current data. Also ***F*** and ***G*** transfer are associated with vertical structures of velocity deviating from its depth-averaged value. These terms, especially ***G***, explained the rest of the contribution of the *Diss* term.

In conclusion, this study shows that tidal dynamics is highly non-linear in the study area. The depth-averaged along-channel momentum balance in the transition zone of the Santee River was estimated. During flood and subsequent current reversal from flood to ebb pressure gradient force is balance by inertia. Meanwhile, during ebb the pressure gradient force is balance by bottom friction, mostly during steady state conditions. The bottom friction is of the leading order in the momentum balance, and tidal dissipation is likely to be also affected by the lateral eddy viscosity. Most of the dissipation occurs during the ebb, when comparable tidal and fluvial currents are additive and subject to the quadratic bottom friction. Highly variable, convergent bathymetry of the transition zone also contributes to the enhanced tidal dissipation through the elevated bottom roughness, tidal

distortion and asymmetry, and possibly by lowering the threshold for flow instabilities and eddy generation.

REFERENCES

Basdurak, N.B., Valle-Levinson, A. (2012). Influence of advective accelerations on estuarine exchange at a Chesapeake Bay tributary. J. Phys. Oceanogr., **42**, 1617–1634.

Blanton, J.O., Lin, G., Elston, S.A. (2002). Tidal current asymmetry in shallow estuaries and tidal creeks. Cont. Shelf Res., **22**, 1731-1743.

Buschman, F.A., Hoitink, A.J.F., van del Vegt, M., Hoekstra, P. (2009). Subtidal water level variation controlled by river flow and tides, Water Resour. Res., 45, W10420, doi:10.1029/2009WR008167.

Dalrymple, R.W., Zaitlin, B.A., Boyd, R. (1992). Estuarine facies models: conceptual basis and stratigraphic implications. J. of Sedimentary Petrology, 62, 1130-1146.

Emery, W.J., Thomson, R. E. (2001). Data Analysis Methods in Physical Oceanography. Elsevier B. V., second ed. Amsterdam, The Nerthelands.

Fong, D., Monismith, S.G., Stacey, M.T., Burau, J.R. (2009). Turbulent stresses and secondary currents in a tidal-forced channel with significant curvature and asymmetric bed forms. J. Hydraul. Eng. 135, 198-208.

Friedrichs, C.T. (2010). Barotropic tides in channelized estuaries, in: Valle-Levinson, A. (Ed), Contemporary Issues in Estuarine Physics, Cambridge University Press, New York, pp. 27-61.

Friedrichs, C.T., Aubrey, D.G. (1994). Tidal propagation in strongly convergent channels. J. Geophys. Res. 99, 3321-3336.

Garvine, R.W., McCarthy, R.K., Wong, K.-C. (1992). The axial salinity distribution in the Delaware estuary and its weak response to river discharge. Estuar. Coast. Shelf Sci. 35, 157– 165.

Geyer, W.R., Trowbridge, J.H., Bowen, M.M. (2000). The dynamics of a partially mixed estuary. J. Phys. Oceanogr. 30, 2035-2048.

Godin, G. (1991). Frictional effects in river tides. In: Tidal Hydrodynamics (Parker, B.B., eds). John Wiley & Sons, New York, NY, USA, pp. 379-402.

Godin, G. (1999). The propagation of tides up rivers with special considerations on the upper Saint Lawrence River. Estuar. Coast. Shelf Sci., **48**, 307-324.

Hoitink, A.J.F., Buschman, F.A., Vermeulen, B. (2009). Continuous measurements of discharge from a horizontal acoustic Doppler current profiler in a tidal river. Water Resour. Res., **45**, W11406, doi:10.1029/2009WR007791.

Horrevoets, A.C., Savenije, H.H.G., Schuurman, J.N., Graas, S. (2004). The influence of river discharge on tidal damping in alluvial estuaries. J. Hydrol., **294**, 213-228.

Jay, D.A. (1991). Green's Law revisited: Tidal long-wave propagation in channels with strong topography. J. Geophys. Res. 96, 20,585-20,598.

Lanzoni, S., Seminara, G. (1998). On tide propagation in convergent estuaries. J. Geophys, Res. 103, 30,793-30,812.

LeBlond, P.H. (1979). Forced Fortnightly tides in shallow rivers. Atmos.-Ocean, 17, 253-264.

Prandle, D. (2003). Relationships between tidal dynamics and bathymetry in strongly convergent estuaries. J. Phys. Oceanogr. 33, 2738-2750.

Prandle, D. (2009). Estuaries: dynamics, mixing, sedimentation, and morphology. Cambridge Univ. Press, New York, USA, 236 pp.

Pritchard, D.W. (1967). What is an estuary: Physical viewpoint, In Estuaries. Ed. G.H. Lauf, 3-5. Washington, D.C.: A.A.A.S. Publication No. 83.

Sassi, M.G., Hoitink, A.J.F. (2013). River flow controls on tides and tide-mean water level profiles in a tidal freshwater river. J. Geophys. Res. Oceans, **118**, doi:10.1002/jgrc.20297.

Savenije, H.H.G., Toffolon, M., Haas, J., Veling, E.J.M. (2008). Analytical description of tidal dynamics in convergent estuaries. J. Geophys. Res. 113.

Schlichting, H., 1960. Boundary Layer Theory. McGraw-Hill Book Company, Inc., New York, NY, USA, 647 pp.

Scully, M.E., Friedrichs, C.T. (2007). The importance of tidal and lateral asymmetries in stratification to residual circulation in partially mixed estuaries. J. Phys. Oceanogr., **37**, 1496-1511.

Seim, H., Blanton, J., Elston, S. (2006). Tidal circulation and energy dissipation in a shallow, sinuous estuary. Ocean Dynamics., 56, 360-375. DOI 10.1007/s10236-006-0078-x

Speer P.E., Aubrey, D.G., Friedrichs, C.T. (1991). Nonlinear hydrodynamics of shallow tidal inlet/bay systems. Edited by B.B. Parker, pp. 321-339, John Wiley, New York.

Stacey, M.T., Brennan, M.L., Burau, J.R., Monismith, S.G. (2010). The tidally averaged momentum balance in a partially and periodically stratified estuary. J. Phys. Oceanogr., 40, 2418-2434.

Trowbridge, J.H., Geyer, W.R., Bowen M.M., Williams III, A.J. (1999). Near-bottom turbulence measurements in a partially mixed estuary: turbulent energy balance, velocity structure, and along-channel momentum balance. J. Phys. Oceanogr. 29, 3056-3072.

Vermaas, D.A., Uijttewaal W.S.J., Hoitink, A.J.F. (2011). Lateral transfer of streamwise momentum caused by a roughness transition across a shallow channel. Water Resour. Res., 47, W02530, doi:10.1029/2010WR010138.

Wong, K.-C., Sommerfield, C.K. (2009). The variability of currents and sea level in the upper Delaware estuary. J. Marine Res. 67, 479-501.

Yankovsky, A.E., R. Torres, L.M. Torres-Garcia, K. Jeon. (2012). Interaction of tidal and fluvial processes in the transition zone of the Santee River, SC, USA. Estuaries and Coasts, **35**, 1500-1509. DOI 10.1007/s12237-012-9535-6.

APPENDIX A – THE PRESENCE OF LATERAL MOMENTUM

We presented in section 3.2, using hydrostatic approximation, the along-channel momentum balance equation (1). This equation can be simplified by assuming that the momentum is diffused by eddy viscosity by a constant value and rewritten as,

$$\underset{\boldsymbol{A}}{\frac{\partial u}{\partial t}} + \underset{\boldsymbol{B}}{u\frac{\partial u}{\partial x}} + \underset{\boldsymbol{C}}{v\frac{\partial u}{\partial y}} = \underset{\boldsymbol{D}}{-g\frac{\partial \eta}{\partial x}} - \underset{\boldsymbol{E}}{\frac{\tau_b}{\rho h}} + \underset{\boldsymbol{F}}{A\left(\frac{\partial^2 u}{\partial x^2}\right)} + \underset{\boldsymbol{G}}{\frac{\partial^2 u}{\partial y^2}} \qquad (7).$$

Here A is the kinetic horizontal eddy viscosity, x and y are long- and across-channel coordinates, respectively. We discussed in section 3.3 that while the depth increases from S to D locations, the depth-average velocity does not decrease. The record-mean discharges through the unit across-channel distance at S, M, and D sites are 0.24, 0.26, and 0.45 m^2s^{-1}, respectively. Since the net discharge integrated across the channel should be conserved, this discrepancy implies that the transverse structure of the along-channel flow changes from site to site with the more laterally uniform current at location S and more jet-like structure at location D. This lack of local along-channel velocity variations in response to the depth change leads us to suggest that the across-channel eddy viscosity ***F*** should contribute to the momentum balance, while ***G*** is likely to be small due to near-uniform *u*.

We estimated the relationship between *Diss* and ***E*** terms and we determined that bottom friction is not the only term responsible for the momentum dissipation. Furthermore, we argue that the other likely candidate is the lateral eddy viscosity in the

cross-channel direction (***G***). We estimated a residual term ***R*** which should be related with the lateral eddy viscosity, and plotted it against all explicitly resolved momentum balance terms (i.e., ***A***, ***B***, ***D*** and ***E***). Only the ***D*** versus ***R*** combination shows a significant linear regression slope (Figure 3.10). We conclude that the along-channel pressure gradient force can trigger the formation of eddies which diffuse momentum in the transverse direction. The peak value of the eddy viscosity coefficient A in (7) can be estimated as follows. We select data points with high absolute values of *Diss* such that $|Diss| \geq 6\times10^{-5}$ ms^{-2} (shown in green in Figure 3.10). For these data points, we obtain the following average values: $Diss \approx -6.8\times10^{-5}$, $\boldsymbol{E} \approx -3.2\times10^{-5}$, and $\boldsymbol{R} \approx -3.6\times10^{-5}$ ms^{-2}; i.e., the residual term magnitude on average exceeds the corresponding bottom friction term magnitude. Next, we assume the transverse structure of the along-channel flow to be triangle-shaped and we approximate the second derivative of the along-channel velocity in the across-channel direction with finite differences as $\frac{\partial^2 u}{\partial y^2} \approx -\frac{16U_c}{W^2}$, where U_c is the scale for the maximum along-channel velocity at the center of the channel, and W is the channel width. We estimate A by solving the following system (approximations for across-channel horizontal eddy viscosity and bottom friction terms):

$$R \sim A\frac{\partial^2 u}{\partial y^2} \approx -A\frac{16U_c}{W^2} \approx -3.6\times10^{-5} \quad (8),$$

$$\frac{C_d U_c^2}{h} \approx -3.2\times10^{-5} \quad (9).$$

Assuming h=3 m, C_d=3×10^{-3}, and W=130 m, we obtain $A \approx 0.2$ m^{2}s^{-1}.